Investigating the Effect of Hydrophobic Nanofillers on Corrosion Protection Performance of Epoxy Coatings on Aluminum Alloy (AA-2219) for Application in Marine Environment

By

Tahseena Khaleeq
Reg.no. 02182113017

Department of Physics
Quaid-i-Azam University

Islamabad, Pakistan

A DISSERTATION SUBMITTED IN PARTIAL FULFILLMENT OF THE REQUIREMENTS FOR THE DEGREE OF MASTER OF PHILOSOPHY IN PHYSICS

(2021-2023)

Declaration

I hereby declare that this thesis **"Investigating the Effect of Hydrophobic Nanofillers on Corrosion Protection Performance of Epoxy Coatings on Aluminum Alloy (AA-2219) for Application in Marine Environment"** neither as a part nor as a whole, has been copied out from any source. It is further declared that the research work presented in this discussion has not been submitted for any other degree or qualification to any other university. If any part of this work is proven to be copied from any source, I, **Ms. Tahseena Khaleeq** (Reg. no.02182113017), shall be legally responsible for punishment under the plagiarism rules of the Higher Education Commission (HEC), Pakistan.

Date: 12/12/2023

Signature of Student

Tahseena Khaleeq

Reg.no. 02182113017

Certification

I have carefully read and approved the thesis titled "**Investigating the Effect of Hydrophobic Nanofillers on Corrosion Protection Performance of Epoxy Coatings on Aluminum Alloy (AA-2219) for Application in Marine Environment**" by Tahseena Khaleeq, Reg. no.02182113017. I recommend this thesis to the Department of Physics for acceptance, as it fulfills the requirements for the degree of Master of Philosophy in Physics.

Date: 12/12/2023

Research Supervisor

_____

Dr. Naveed Zafar Ali

Experimental Physics Directorate,

National Centre for Physics (NCP),

Islamabad, Pakistan

Submitted through:

Head of Department

_____

Dr. Kashif Sabeeh

Department of Physics,

Quaid-i-Azam University Islamabad,

Pakistan

Dedication

This thesis is dedicated to my beloved parents

Acknowledgments

In the name of **ALLAH**, the Most Compassionate, the Most Merciful. All praise and gratitude belong to **ALLAH**, the source of all knowledge and wisdom. I extend my deepest appreciation to the **Holy Prophet Muhammad (peace be upon him)**, whose life remains an eternal beacon of guidance and enlightenment for all of humanity.

My sincere gratitude is extended to **Dr. Naveed Zafar Ali** of the EPD Department at the National Centre for Physics, Quaid-i-Azam University Campus, Islamabad. His unwavering guidance, invaluable support, and constant motivation have been instrumental in shaping the trajectory of my MPhil project. With his dedicated mentorship, I have been able to navigate challenges and successfully bring my project to fruition.

Above all, my deepest and most profound gratitude goes to my **beloved parents and siblings**. Their unwavering support, benevolent blessings, and sincere prayers have been my guiding light throughout this journey. Their faith in me has been an unshakable foundation upon which I've built my academic pursuit.

Tahseena Khaleeq

Table of Contents

List of Figures

List of Tables

Abstract

Corrosion is a universal issue that impacts many industries, particularly for ships and submarines in oceanic environments. The present study examines the influence of adding hydrophobic nanofillers into epoxy coatings on aluminum alloy (AA-2219) surfaces to improve their corrosion protection performance in seawater. The aim of the research is to find out the impact of a series of Zeolitic Imidazole Framework (ZIFs) nanofillers and their composites with Tetraethyl orthosilicate (TEOS) which is a hydrophobic and crosslinking agent in augmenting the coating's capacity to resist corrosion that sustain the harsh conditions encountered in maritime environments. In the present work, we have prepared a series of hydrophobic nanofiller epoxy-based coatings namely (a) Pure epoxy, (b) ZIF-67+Epoxy, (c) ZIF-67@TEOS+Epoxy(6w%), (d) ZIF-67@TEOS+Epoxy(10w%). The material was analyzed using various techniques including Fourier-transformed infrared spectroscopy (FT-IR) confirming the characteristics vibrational modes ascertaining the formation of ZIF-67 nanoparticles. The peak at 423 cm^{-1} is associated with the Co-N stretching vibration that confirms the Co-N bond formation within the ZIF-67 architecture. The crystallinity, purity and average crystallite size of the synthesized material are confirmed by XRD. The unique diffraction peaks of ZIF-67 reveal its high purity and crystallinity. Scherrer's equation is used to calculate the average crystallite size of the ZIF-67 NPs. The average crystallite size is measured to be 0.0984 nm. The comparison of ZIF-67 with a series of different coated coupons indicates that its crystallinity transforms into an amorphous state. The elemental composition, chemical, and electronic state of atoms in a material was analyzed through XPS. The spectrum predominantly exhibits peaks at binding energies of 284 eV (C1s), 399 eV (N1s), 532 eV (O1s), and 791 eV (Co 2p), which provide further evidence for the successful formation of ZIF-67. SEM images combined with EDX analysis provide information regarding the surface properties of the material, including its composition, morphology, and topography. Average particle size was also calculated through SEM by using Image J which is 310.85 nm as reported. Employing electrochemical impedance spectroscopy (EIS) and Tafel, electrochemical techniques on the bare aluminum alloy (AA-2219), and a series of different coated samples were carried out to evaluate the corrosion resistance (R_{corr}), pore resistance (R_{po}), solution resistance

(R_{soln}), corrosion current (I_{corr}), corrosion potential (E_{corr}) and corrosion rate at a different time interval. Electrochemical studies revealed that ZIF-67@TEOS+Epoxy(6w%) is the best composite anticorrosive coating having superior corrosion resistance amounting up to 27,780 ohms for two weeks of immersion in 3M NaCl solution compared to the other coated samples. ZIF-67@TEOS+Epoxy (6w%) has greater corrosion resistance throughout the time interval from one week to three months. The Tafel scan demonstrated a significant decrease in corrosion rate for ZIF-67@TEOS+Epoxy(6w%) which is 0.2334 mpy for two weeks of immersion in 3M NaCl solution. This is because ZIF-67 possesses the ability to adsorb corrosive species due to their high surface area and adjustable pore sizes. ZIF-67-containing coatings have the ability to reduce the concentration of species at the metal surface, which slows down or prevents the corrosion process. It also accelerates the curing reaction of epoxy which increases its corrosion protection performance. The employment of TEOS facilitates effective bonding between the organic and inorganic phases, thereby preventing phase separation. ZIF-67 has a high surface area and adjustable pore size that provides channels to TEOS which is a cross-linking agent that increases corrosion resistance. This research will boost corrosion protection technology by improving epoxy coatings for aluminum structures in marine settings.

Chapter 1

1. Introduction

1.1. Aluminum and its Alloys

Aluminum is the most common metallic element and is typically found in rocks like bauxite and cryolite. Aluminum has been produced more frequently and is used in a wide range of applications. Aluminum boasts an unparalleled combination of characteristics, encompassing a featherweight quality with a slight density of roughly 2.7g/cm3, immunity to corrosion, eminent heat and electricity conductivity, remarkable reflectivity, effortless malleability and machining, non-toxic and transparent properties of its corrosion byproducts, economical and abundant availability, recycling capabilities, and an array of other advantageous qualities that further establish its suitability for employment in marine settings [1]. Aluminum is a silvery-white metal. It is bendable and soft. The addition of various alloying elements to aluminum resulted in a wide range of industrial uses [2]. The versatile aluminum alloys have a multitude of applications and usages spanning across various fields. They are utilized in engineering for fabricating machined components and electro-mechanical components. Furthermore, they are also used for crafting cooking utensils, building and construction of windows, doors, siding, building wire, sheathing, and roofing. In addition, they are employed in the food industry for storage and packaging of cans, foil, and frames. The transportation industry also benefits from the aluminum alloys as they are utilized in automobiles, aircraft, trucks, railway cars, marine vessels, bicycles, spacecraft, and many more areas [3].

An alloy is a metal created by mixing two or more metallic components, typically to increase strength or corrosion resistance. In comparison to pure metal, an alloy possesses superior qualities. Pure metals tend to be soft, flexible, and corrosive [4]. The addition of additional materials can strengthen the corrosion resistance of pure metal. Among others, silicon, magnesium, manganese, copper, and zinc are some of the principal alloying elements. Wrought aluminum alloys are classed according to the nature of the primary alloying constituents, as shown in Table 1. The primary alloying elements of the series are used to give the first digit of a four-digit system. The second digit is based on changes to

impurity limitations, while the third and fourth digits are based on the particular alloy in the series [5].

1.2. Different types of Aluminum Alloy

Due to their exceptional ratio of strength to weight and endurance against fatigue, the heat-treatable aluminum alloys belonging to the 2xxx family (of the Al-Cu type) are frequently employed for structural purposes, particularly in the aerospace and automotive domains, where moderate service temperatures are common. The mechanical properties of such alloys are achieved through the phenomenon of precipitation (or age-hardening) hardening, wherein the existence of an orderly precipitate structure leads to an increase in strength [6]. The alloying components are totally dissolved in a solid solution, which causes the material to act as a single-phase material with weak mechanical properties. According to the aging temperature, the alloying components cluster and begin to form various forms of tiny precipitates. Conventional testing methods like micro-hardness, stress testing, and optical or electron microscope scanning are typically used to determine and qualify the mechanical properties and microstructures that result after solution treatment and aging [7]. These evaluation methods are time-consuming, expensive, and damaging by nature. Additionally, it is assumed that these tests are performed on "coupon samples," which are actually accurate representations of the element that will be put into service. The traditional "coupon-based" method of assessing material qualities could not be adequate since there might be differences between the component's actual heat treatment and the heat treatment observed by the coupon [8]. Therefore, it's possible that the findings of destructive testing on coupons don't actually relate to the component that will be put to use. Additionally, when these alloys are used in service at temperatures between 130 and 170 °C, which are close to those used for fake aging treatment, the aging procedures continue, over-aging the material (causing precipitates to become coarser), and degrading its mechanical properties like hardness and tensile strength [9].

Table 1:1: Classification of aluminum alloys

Aluminum-Alloy series	Principle alloying elements
1xxx	Pure aluminum (Al)
2xxx	Copper (Cu)
3xxx	Manganese (Mn)
4xxx	Silicon
5xxx	Magnesium (Mg)
6xxx	Magnesium and Silicon
7xxx	Zinc (Zn)
8xxx	Other elements (Sn (Tin), Lithium (Li), and Iron (Fe)

The wrought aluminum alloys can be divided into heat-treatable and non-heat-treatable alloys. Heat treatment can create the precipitate phase, resulting in high strength values for heat-treatable alloys [10]. The primary precipitation-hardening aluminum alloys are the 2xxx, 6xxx, 7xxx, and some 8xxx series. Non-heat-treatable alloys are hardened through cold working only. Al-Mg alloys from 1xxx, 3xxx, and 5xxx series are non-heat-treatable. Al-Si alloys from the 4xxx series may or may not be heat-treatable [11].

1.3. Metal-Organic Framework (MOFs)

Metal-organic frameworks (MOFs) are widely recognized as a prominent class of materials that exhibit enormous potential for various material advancements in multiple fields, such as electronics, smart devices, catalysis, sensors, and separation technology. These materials are renowned for their distinctive morphology, structure, porous nature, and vast surface area, which are the main features that draw attention towards them. Metal-organic frameworks are porous materials made from metal-containing nodes and organic linkers (Fig.1). These materials are also known as PCPs or SBUs. MOFs are exciting materials with adjustable structures and functions. Chemistry is seeing rapid growth in this area [12]. Porous materials have received an extensive amount of interest in several fields of study over the last three decades, including physics, chemistry, and material science. Porous

materials serve important roles in our daily activities, with widespread applications in adsorption, separation, biomedicine, and catalysis [13]. Traditional porous materials, such as activated carbons and zeolites, have found widespread practical uses due to their low cost and improved stability, but they nevertheless suffer from issues like non-uniform structure, uneven pores, and a lack of transparent structure-property connections. As a result, scientific research into better-performing enhanced porous materials for various applications remains active [14]. Metal-organic frameworks, stunning hybrid materials, are made up of metal ions and organic linkers. These ions form nodes that create a cage-like pattern. MOFs have an impressive interior surface area due to their unique structure [15]. Metal-organic frameworks (MOFs) have revolutionized the world of porous substances in the past 20 years. They are formed by coordinated bonds between metal ions/clusters and organic connectors through reticular synthesis.

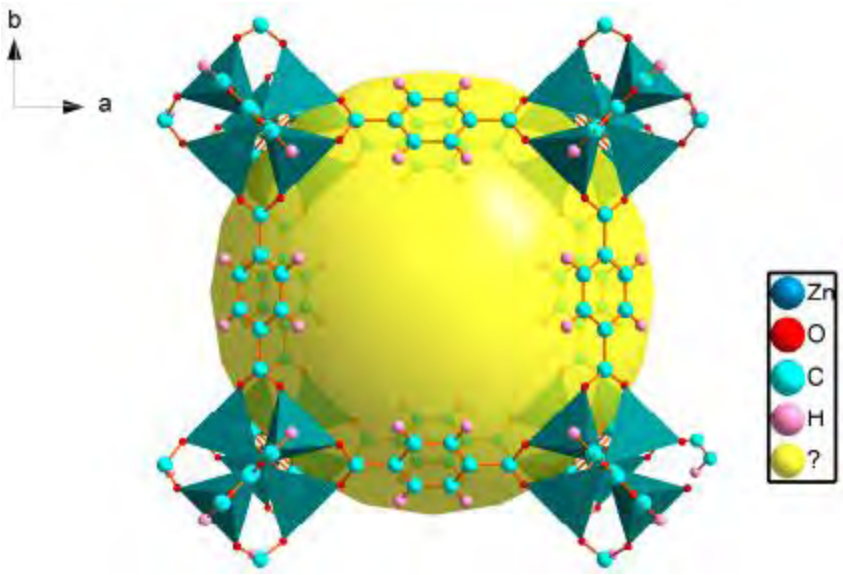

Figure 1:1: Structure of MOF-5

MOFs of crystalline nature typically have exceptionally high surface areas (normally in the range of 1000 to 10 000 m^2/g) and adjustable pore sizes/characteristics due to the flexibility of the constituents' shape, size, and functionality. MOFs have high porosity (90 percent free volume), design flexibility, crystalline nature, distinctive morphologies, and a synergistic mix of inorganic and organic components [17]. These characteristics encourage

MOFs with incredible functionalities/properties for a wide range of applications, including adsorption of gas and separation, catalytic reactions, detectors, delivery of medication, proton conduction, and so on. One of the fundamental problems for diverse MOF applications is stability, which includes chemical, thermal, and mechanical stability [18]. The study of MOFs has advanced significantly over the last 20 years and is still expanding quickly, with thousands of publications being produced annually. The complete pore size gap between mesoporous silicas and microporous zeolites can be filled by MOFs thanks to their diverse structural makeup and highly adjustable pore diameters (typically 0 to 3nm, up to 9.8nm) [19]. One may readily adjust the compositions and architectures of MOFs to precisely obtain the desired functionality thanks to the wide diversity of metal nodes and the theoretically limitless number of organic linkers. Additionally, the clear structure-property relationships that can be established on MOFs thanks to their well-defined and flexible crystalline structures are ideal for phenomenological agreement and serve as guidelines for the creation of new functional materials. In this study, we first go over the special structural benefits of MOFs as well as their physical characteristics, such as stability, pore characteristics, and surface area, for practical applications [20].

In the last two decades, numerous unique constructions were discovered. However, MOFs are typically unstable in various areas such as water, acid/base, heat, and mechanical [21]. However, MOF stability is vital for many practical applications. Significant progress has been made in addressing this challenge through various efforts. As MOFs degrade in water or water vapor, substitution processes swapping metal-coordinated linkers with water or hydroxide can be observed. Thus, enhancing coordination bonds between SBUs and organic linkers is the key strategy for improving MOF stability [22].

1.3.1. Zeolitic Imidazolate Framework (ZIF)

ZIFs are a subclass of Metal–organic framework (MOF) compounds that involve M-Im-M (where M represents Zinc and Cobalt and Im represents imidazolate linker) constructed through a self-assembly methodology. The remarkable characteristics of ZIF, notably its expansive surface areas, voluminous pores, and customizable pore sizes, have captured the attention of many scholars, rendering it a fascinating area of research [23]. Zeolitic imidazolate frameworks (ZIFs) are popularly studied MOFs due to their simple synthesis,

customizable features, stability, and porosity. Zeolitic Imidazolate Frameworks (ZIFs) have made significant contributions to diverse fields such as gas storage, gas separation, catalysis, sensing, CO2 capture, and the removal of heavy metals. These frameworks have proven to be versatile and effective in addressing a variety of challenges in the areas mentioned above [24]

1.3.1.1. Zeolitic Imidazolate Framework (ZIF- 67)

There exist several subclasses of Metal-Organic Frameworks (MOFs), which are dependent upon the presence of the metal cation and organic ligand. Among these, ZIF-67 stands out as one of the most extensively utilized MOFs for a range of applications where it acts as a soft template. Zeolitic imidazolate frameworks are highly stable MOFs, especially ZIF-67. ZIF-67 is a cobalt MOF with a uniform structure of cobalt ions and 2-methyle imidazole linkers. Each cobalt ion is linked to four nitrogen atoms from four 2-methyle imidazole ligands. Each 2-methyle imidazole ligand links two cobalt center [25]. Zeolitic imidazolate frameworks such as ZIF-67 are highly stable MOFs, featuring a uniform structure of cobalt ions and 2-methyle imidazole linkers that are interconnected through coordination bonds [26]. ZIF-67, a cobalt MOF with stable zeolitic imidazolate frameworks, is formed by cobalt ions linked to 2-methyl imidazole linkers [27]. ZIF-67, a stable and uniform cobalt MOF, is composed of cobalt ions and 2-methyl imidazole linkers where each ion links to four nitrogen atoms and each ligand links two cobalt centers [28],[29].

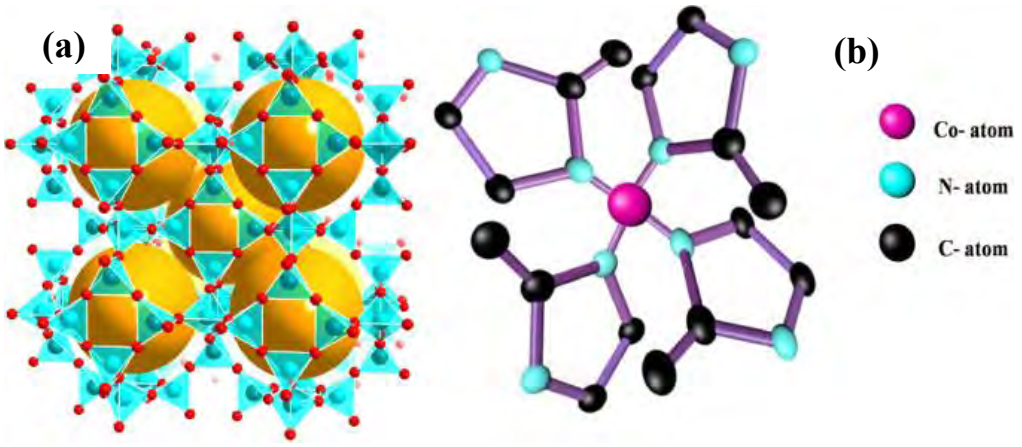

Figure 1:2: (a) sodalite structure, (b) cobalt ions coordinated by 2-methylimidazolate ligands through nitrogen atom of imidazole ring.

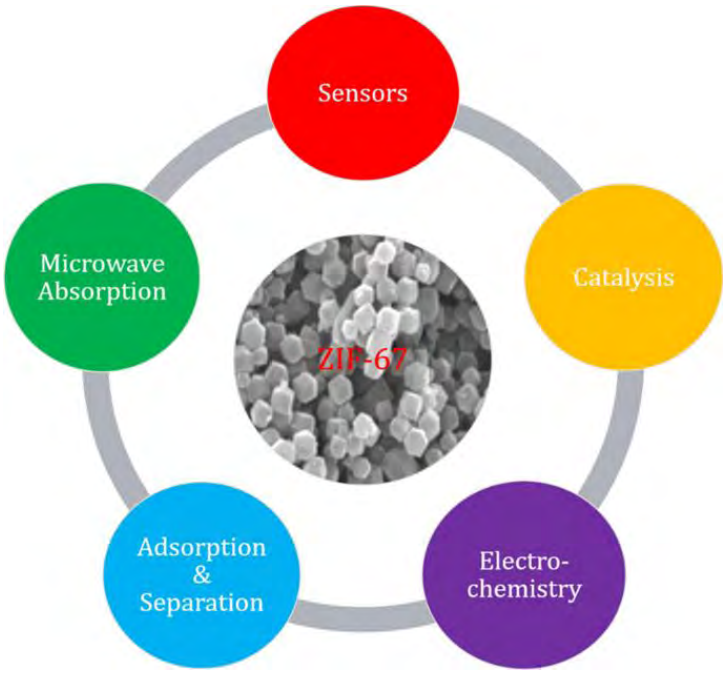

Figure 1:3: ZIF-67 and its applications [30].

Cobalt and the compound 2-methyl imidazole possess remarkable properties as corrosion inhibitors, capable of expediting the curing reaction of epoxy. Using ZIF-67 in epoxy can provide great anti-corrosion ability, but its high water solubility and hydrophilicity pose challenges in inhibiting ZIF-67 particles in aquatic environments [31].

1.4. Epoxy

Epoxy is a versatile family of basic components and cured products. It's a class of reactive prepolymers and polymers that contain epoxide groups, also known as poly-epoxides. These groups are collectively called epoxy. Epoxy resins can bond with themselves or other substances through catalytic reactions. These substances include polyfunctional amines, acids, phenols, and alcohols. Hardening agents or curatives are often called co-reactants, while the process of cross-linking is referred to as curing [32]. When poly-epoxides react with themselves or with polyfunctional hardeners, a thermosetting polymer is created. This polymer usually has excellent mechanical properties and can withstand high temperatures and chemicals. The properties of epoxy resins span a wide spectrum, encompassing low-viscosity liquids all the way to high-melting solids. These resins may exhibit aromatic or aliphatic traits, as well as cyclic or acyclic structures. Furthermore, they possess the ability to be either monofunctional or polyfunctional. [33]. Because of their versatility, epoxy resins stand out as a significant class of polymers. Although this is the case, epoxies are virtually ever discussed in Materials Science and Engineering textbooks, leaving students unprepared for the wide range of applications for these materials. The hardened epoxies have several favorable properties due to the high degree of crosslinking and the structure of the interchain links [34]. High strength (tensile, compressive, and tensile), great adherence to numerous surfaces, and resistance to chemicals, fatigue, corrosion, and electricity are some of these qualities. By choosing the right epoxy monomer and curing agent or catalyst, it is possible to maximize both the end attributes of cured epoxies, like strength or electrical resistance, as well as the processing properties of uncured epoxy resins, such as viscosity. Epoxies are frequently used for coatings, corrosion protectants, electrical encapsulants, fiber optic sheathing, flooring, and adhesives due to their simplicity of use and advantageous qualities [35]. Epoxies were a natural selection for matrices in fiber-reinforced composites because they had the qualities, such as liquid processability and cured strength control, that lead to effective adhesives and coatings. A number of epoxide functional groups located inside the polymer chain are a defining characteristic of epoxies. The three-membered ring comprising one oxygen and two carbon atoms makes up the planar epoxide group, which has a planar structure. The group is highly reactive as a result of the high ring strain, which is comparable to that in cyclopropane [36]. Epoxy is

versatile and used for metal coatings, composites, electronics, electrical components, LEDs, insulators, paint brushes, and plastic materials. Epoxy resin is popular in industries because of its excellent mechanical properties. It has exceptional strength, good insulation, high chemical resistance, and dimensional stability. Its high adhesive and cohesive strength make it suitable for coatings in aerospace, automotive, and electronic industries [37]. Its application areas are continually expanding. It serves as a safeguard for metal surfaces, shielding them from the corrosive effects of rust, oil, and other chemical reactions that may lead to perilous outcomes. The potential of the epoxy-based coating to perform is greatly amplified through the amalgamation of functional fillers. This results in its efficient utilization for the dual purpose of corrosion protection and anti-fouling, particularly in the challenging marine environment [38].

Uncured epoxy resins' physical characteristics can differ greatly. Like any polymer, the molecular weight and molecular structure affect the viscosity of the monomers or prepolymers. The viscosities of higher linear molecular weight monomers, or those with higher values of n, are higher [39]. The density of the resin will also be greatly affected by molecular structure and bond types. Epoxies are nearly always used when combined with accelerators, crosslinking agents, catalysts, and other additives, therefore viscosity effects such as plasticity must be taken into account [40].

1.5. Corrosion

Materials, often metals, degrade over time due to chemical or electrochemical reactions with their surroundings - this is known as corrosion. The natural process of corrosion changes metals into more chemically stable oxides. Metal reacts with oxidants like oxygen, hydrogen or hydroxide via electrochemical oxidation. Electrochemical corrosion includes rusting, which is the formation of iron oxides. Corrosion is possible in non-metallic substances like ceramics and polymers. Corrosion is caused by a redox reaction.

$$2\,Fe + 2\,H_2O + O_2 \longrightarrow 2\,Fe(OH)_2$$

This reaction includes the reduction of oxygen, the dissolution of iron, and formation of rust:

$$Fe \longrightarrow Fe^{2+} + 2\,e^{-} \text{ (anodic)}$$

$$2\,H_2O + O_2 + 4\,e^{-} \longrightarrow 4\,OH^{-} \text{ (Cathodic)}$$

$$Fe^{2+} + 2\,OH^{-} \longrightarrow Fe(OH)_2 \text{ (Chemical)}$$

Figure 1:4: Corrosion of metals [41].

The decay of materials and structures caused by corrosion affects their strength, look and ability to absorb liquids and gases [42]. Structural alloys can corrode due to air moisture and certain substances can strongly affect the process. Corrosion can create localized pits or cracks, or affect a wide area. It happens on exposed surfaces due to diffusion control. By minimizing surface activity, corrosion resistance in materials can be improved through passivation and chromate conversion. Yet, some corrosion mechanisms are still unpredictable and hard to detect. The phenomenon of corrosion is electrochemical and has a complex chemistry [43].

1.5.1. Theories of Corrosion

The process of corrosion is explained by various hypotheses. The next sections go through the thermodynamic and electrochemical theories.

1.5.1.1. Thermodynamic Theory

The corrosion cycle, which is a component of thermodynamic theory, is frequently used to introduce corrosion theory. This means that all metals are unstable when they are in their elemental states. Corrosion is the process by which they stabilize (compounds transform into ores). It has been said that corrosion is extractive metallurgy in reverse and that it is impossible to change the basic rules of thermodynamics in order to prevent corrosion [44].

1.5.1.2. The Electrochemical Theory

This theory states that corrosion is an electrochemical reaction that needs an electron flow to take place. The process begins when water and oxygen pass through an outer layer and reach the metal's depth. Once the electrical current can flow through the water, a reduction process begins in which oxygen combines with the water to form hydroxyl ions (OH-). The cathode is the location where reduction takes place, whereas the anode is the location where oxidation takes place [45].

1.5.2. Forms of Corrosion

Some of the corrosion categories are as follows.

1.5.2.1. Crevice Corrosion

Whenever there is a variation in ionic concentration between two areas of a metal, crevice corrosion may occur. Crevices are where this form of corrosion is most likely to occur, such as in gaskets, washers, and bolt heads. All aluminum and stainless steel grades experience crevice corrosion due to differential aeration cell formation, leading to corrosion in crevices [46].

1.5.2.2. Stress Corrosion Cracking

Stress corrosion cracking (SCC) is the term used for metal cracking due to corrosive surroundings and tensile stress, which usually happens at high temperatures [47].

1.5.2.3. Intergranular Corrosion

The occurrence of intergranular corrosion is due to impurities present in the grain boundaries that separate the metal alloy. It can also happen by the depletion or enrichment of the alloy at these grain boundaries. IGC affects Aluminum-base alloys [48].

1.5.2.4. Galvanic Corrosion

When two metals with different electrochemical properties come into contact in an electrolytic environment, galvanic corrosion may occur. The phenomenon being referred to is the corrosion of a metal at a joint or junction. An example of such corrosion is the degradation of copper when it comes in contact with steel in a salt-water setting [49]

1.5.2.5. Pitting Corrosion

Pitting corrosion is challenging to identify due to its unpredictability and is regarded as one of the most hazardous forms of corrosion. At a specific location, a corrosion cell forms within the metal surface resulting in a pit that can take various shapes. The pit will continue to grow. The metal is being slowly penetrated by the pit in a vertical orientation, which, if left unchecked, can result in structural failure. If left unchecked, this can eventually cause structural failure [50].

1.5.2.6. Uniform Corrosion

The most common type of corrosion occurs when the metal surface is damaged by the atmosphere. - It's easy to see how far the corrosion has spread. - This type of corrosion doesn't affect the material's performance much. - Zinc and steel will dissolve at the same rate when submerged in dilute sulfuric acid [51].

1.5.2.7. Microbial Corrosion

Microbial corrosion, caused by microorganisms, is a form of corrosion also known as microbiologically influenced corrosion (MIC). Chemoautotrophs are the most common type. Corrosion can affect both metallic and non-metallic materials with or without oxygen [52].

1.5.2.8. High-temperature Corrosion

High-temperature corrosion is the corrosion of materials caused by heating. Metal may undergo chemical deterioration from exposure to gases like oxygen, sulfur, or other compounds in a hot environment. The mentioned compounds can easily oxidize materials, specifically metals. Materials in car engines must endure high temperatures for prolonged periods and withstand corrosive combustion products [53].

1.5.3. Conditions of Corrosion

1. There must be an electrochemical response at the metal-environment interface.
2. The potential gradient of two adjacent locations.
3. The cathode and anode need to be electrically connected.
4. Exposure to marine water, a typical electrolyte [54].

When exposed to seawater or wet environments, specialized marine-grade metals are required to prevent failure. These materials must endure the harsh effects of seawater, protected by unique metal components to avoid corrosion [55].

Marine-grade metals include:

- Aluminum
- Stainless Steel
- Copper
- Bronze
- Brass
- Galvanized Steel [56].

1.5.4. Sea water composition

Marine water is a complex solution of inorganic, organic, and biological components, as well as a mixture of various salts such as chlorides, sulfates, and carbonates. Contact with saline water frequently produces corrosion, which leads to the breakdown of materials and affects their qualities [57].

1.5.5. Marine corrosion

Seawater corrosion occurs due to a difference in potential at the metal-environment interface. It is also known as aqueous or marine corrosion. The process is electrochemical and happens at a given pH level of seawater [58]. Metallic components are widely used in the water business. It is the degradation of a substance caused by chemical interaction with the environment. It involves the degradation of polymers, wood, and concrete, as well as metal, which is usually iron (as steel) [59].

Figure 1:5: Marine corrosion [60]

1.5.6. Mechanism of marine corrosion

The corrosion of materials can significantly impair their functionality. When iron and steel undergo decrepitude, they form ferrous oxide (rust), which is a well-known result of corrosion. Other metals corrode differently. The thermal stability and thermodynamic vulnerability of metals against corrosive environment are determined by the Galvanic series of metals. (*The term "passive" refers to the layer of oxide formed naturally on a metal surface, while "active" refers to direct exposure to a corrosive environment.)

Table 1:2: Galvanic series of metals in seawater

Anodic (active*)	Stainless Steel (passive*)
Magnesium	Gold
Aluminum	Graphite
Zinc	Platinum
Mild Steel	Cathodic (Noble)

Cast iron Stainless steel (active) Copper	

1.5.7. Factors affecting marine corrosion

There are numerous factors that influence the rate of corrosion. Some of these are listed below:

1. Metal Reactivity.
2. The presence of electrolytes in water.
3. Presence of dissolved gases, primarily carbon dioxide.
4. Temperature, pH, and UV light.
5. Biological impurities that speed up deterioration [61].

1.5.8. Corrosion prevention methods

1.5.8.1. Barrier coatings

To avoid corrosion, a cost-effective method is to apply barrier coatings such as paint, plastic, or powder. Barrier protection creates a thin layer that shields the metal alloys by separating the metal substrate from the corrosive environment. Powder coatings, such as epoxy, nylon, and urethane, attach to the metal surface to form a thin layer. Plastic and waxes are frequently applied on metal surfaces. Paint functions as a protective layer against electrochemical charge that arises from corrosive compounds on the metal surface [62]. Today's painting systems consist of various layers with distinct purposes. The first coat inhibits, the second coat increases thickness, and the final coat protects against environmental factors. The main disadvantage of coatings is their frequent need for stripping and reapplication. Improperly applied coatings may result in corrosion. Coatings are hazardous to humans and the environment due to their volatile organic compound content [63].

1.5.8.2. Cathodic Protection

Cathodic protection prevents corrosion through electrochemical methods. Electron supply from galvanic anodes creates passive sites to transform active sites in metals. Cathodic

protection process uses aluminum, magnesium or zinc as anodes [64]. Although cathodic protection is a reliable method, the anodes themselves have a limited lifespan and necessitate frequent inspections and replacements, resulting in increased maintenance expenses. Adding them can make the structure heavier - They might not work well in areas with high resistance [65].

1.5.8.3. Hot-Dip Galvanization

A technique to prevent corrosion by immersing steel into molten zinc, creating a strong alloy coating for protection. The ancient method of galvanization is used to prevent corrosion on sculptures and playground equipment. However, it requires removal of the equipment making it impractical to use on-site. The process may not be feasible for larger equipment, causing companies to abandon it [66].

1.6. Coating Techniques

1.6.1. Dip Coating

A budget-friendly method produces consistent top-notch coating on diverse shaped and sized bases, even on extensive surfaces. Dip coating can be done by hand or machine to meet high production demands. Objects are dipped in a polymer tank and taken out at a fixed speed with monitored temperature and atmosphere [67]. The determination of coating thickness is influenced by several factors such as the coating viscosity, immersion duration, withdrawal rate and number of dipping cycles. Solidification commonly happens in an oven at high temperatures. Before dip coating, surfaces must be clean from pollutants. Process control and consistent quality control standards require suitable flow and run off properties [68]. During dip coating, both internal and external surfaces are coated simultaneously. The coating grades are durable, transparent, have minimal resistance, protect from corrosion coating is applied to the center of the substrate and spun rapidly using centrifugal force. The spin coater is rotated until the desired thickness is achieved substances, withstand shock and vibration, and possess excellent electrical insulation properties [69].

Figure 1:6 :Dip Coating [70]

1.6.2. Brushing

The application of coating requires skilled personnel and appropriate brush to ensure efficient distribution of liquid polymer. The application of multiple coats may be necessary for achieving the desired film thickness. It is crucial to ensure that the bristles of the brush being used are compatible with the product [71].

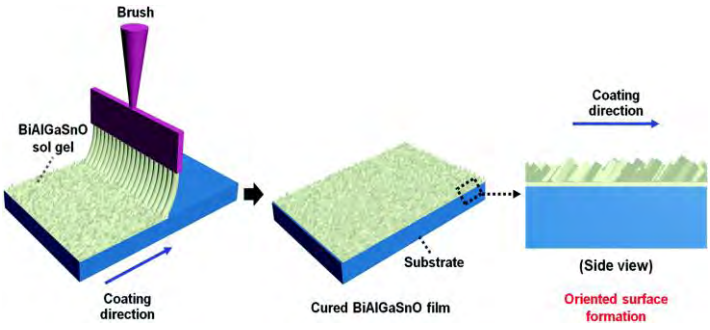

Figure 1:7: Coatings through brushes [72]

The size, shape, and angle of the brush should be taken into consideration when covering irregular surfaces such as edges, corners, boltheads, welds, and piping. Prior to use, it is

important to clean the brushes. Although brushing has a brief preparation period, it is comparatively sluggish when compared to other coating methods. Advantages include minimal waste, modest capital expenditure, and financial suitability for brief production cycles [73].

1.6.3. Roll Coating

Paint rollers are utilized for manual painting of expansive level spaces. For best outcomes, it is important to use top quality roller covers and frames. The roller coating method offered by Master Bond is quicker than brushing, but it is not suitable for bumpy or textured surfaces. Additionally, it is challenging to regulate the thickness of the film using a paint roller. Automated roll coating equipment can apply liquid polymeric coatings uniformly to flat surfaces for high volume production through direct roller coaters and reverse rolling machines [74].

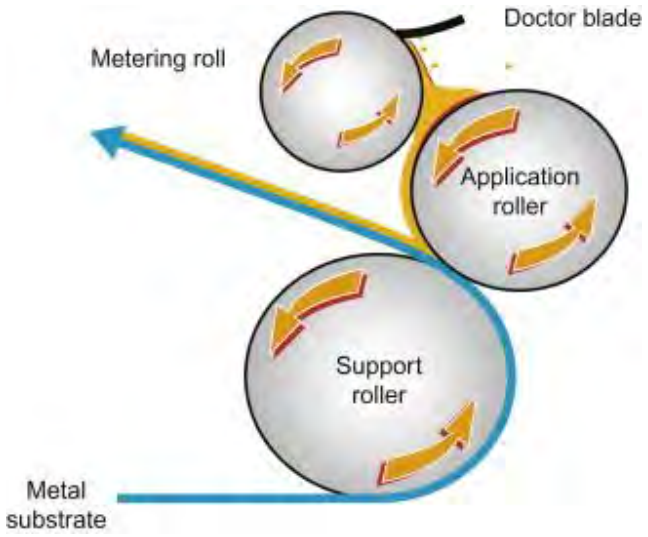

Figure 1:8: Roll Coating [75]

The selection of the appropriate machine depends on factors such as the substrate type, thickness/width, and coat type. There are various roll coaters with different configurations to choose from to meet diverse needs, while providing cost-effective and reliable high-quality finishes. This widely used energy-saving process is characterized by low labor

requirements, reduced waste, high coating transfer efficiency, precise weight control, and design versatility [76].

1.6.4. Spray Coating

A multifunctional and cost-effective coating method is available for various types of parts, including large surface areas. High-quality finishes can be achieved through manual or automatic application of viscous or non-viscous liquid coatings with high transfer efficiency. Various kinds of spray guns and equipment, such as airless spray, air atomized conventional sprays, air assisted airless sprays, are available to meet specific requirements of material use, desired film thickness, quality of finish, reduction of overspray, edge buildups, wasted product concerns, and reliable performance [77].

Figure 1:9: Plasma Spray Coating [78]

The control of spray patterns and delivery rates rely on the coating characteristics. Fluid delivery can be adjusted to compensate for seasonal changes in temperature and humidity, and to enable spraying in recesses and cavities. Spraying has the benefit of being able to be done from a vertical angle, and it also contributes to a secure work setting. There are several common issues with spray coatings, such as sagging, orange peel, and overspray. It's important to follow proper control features for good atomization and flow. To achieve defect-free coatings and high transfer efficiency, precise application techniques are necessary, including the use of the best spray pattern, distance, and angle [79].

1.6.5. Spin Coating

A coating is applied to the center of the substrate and spun rapidly using centrifugal force. The spin coater is rotated until the desired thickness is achieved. The crucial elements for fulfilling specific application needs are viscosity, rate of spinning, spin time, acceleration, surface tension, resin materials, and substrates. Spin coating has demonstrated exceptional efficacy in delivering uniform and consistent thin coatings, without any variation in thickness or quality of finish. The spin coating process is straightforward, fast, and applicable to both small and large substrates. The issues that can arise during processing are swirl patterns, uncoated areas, comets, streaks, and films that are too thin or too thick. The use of nanosilica filled systems has been important in improving the quality of ultrathin films [80].

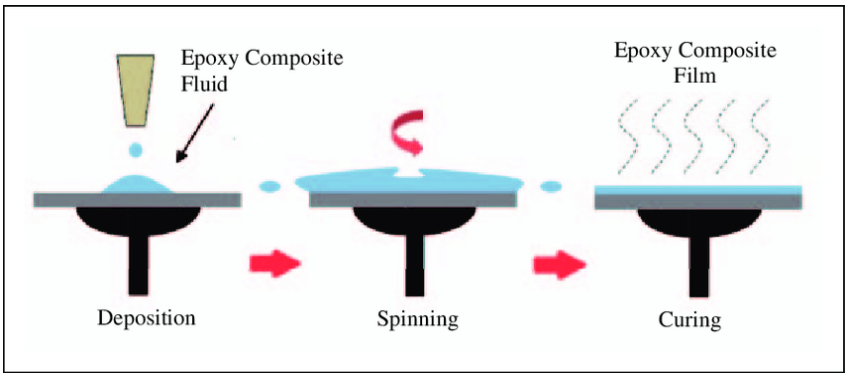

Figure 1:10: Spin Coating process [81]

1.6.7. Flow Coating

Flow coating is a dependable and efficient technique to apply liquid coatings manually or automatically. Its use is suggested for large, flat, horizontal sheets, and panels that are not easy to dip coat. Furthermore, it is possible to achieve significant coating thicknesses using a solitary coat. The process of flow coating is cost-effective, occupies minimal space, reduces waste and provides high transfer efficiency [82]. Coatings are intended for application on the upper part of objects and will spread out to cover flat surface areas. The rate of flow is dependent on the compound's viscosity. The finish and uniformity can be

affected by curing conditions such as temperature and humidity. Flow coating is unsuitable for objects with holes or pultrusions [83].

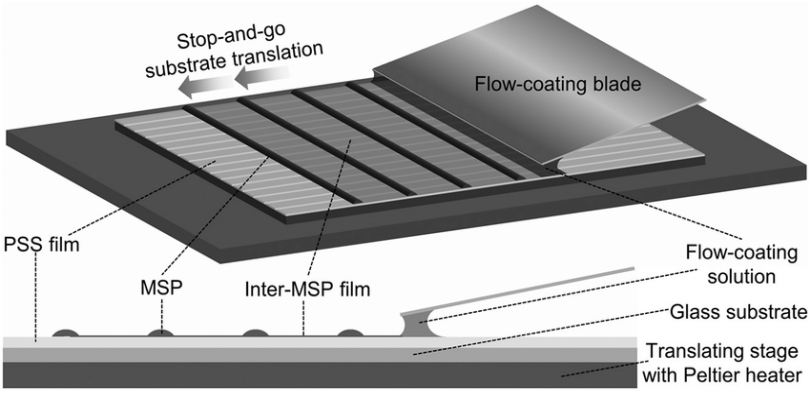

Figure 1:11: Schematic representation of flow-coating process [84]

1.7. Anticorrosion coatings

Surface treatment, such as applying protective coatings, is another effective way to shield metals from an aggressive environment. These coatings serve a dual purpose by serving as both a physical barrier against corrosive chemicals and an electric fence between the environment and the metal interface. However, when exposed to the outside environment, these protective layers are vulnerable to damage that can lead to the development of cracks, some of which are imperceptible and contribute to the acceleration of corrosion. Few times in the past have both organic and inorganic coatings been used to keep metals from corroding. Despite advancements in coating technology, using different alloys for long-term metal protection is still a major challenge for corrosion scientists [85]. The limited availability of highly effective anticorrosion coating systems and the shortening of their useful life are caused by the complexity of the substrate/coating system and various other factors. In addition to composition, which consists of binders, extenders, solvents, and pigments, several other factors, such as coating thickness, curing, substrate preparation, adhesion between the coating layer and the substrate, and environmental restrictions, also have an impact on coating performance [86]. An efficient coating must have good adherence to the substrate, be flexible, be tough enough to survive breaking and maintain

its appearance even when subjected to mechanical stress, corrosion, and stress. European and country legislation have agreed to develop the coating sector through constant technological progress, phasing out the usage of voltaic organic compounds in favor of powder coatings or water-borne coatings, which will improve the formulation of anti-corrosive coatings. Therefore, the marine sector needs comprehensive knowledge of and comprehension of interactions between various coatings' components. The physical or chemical processes that cause coatings to fail may provide a path to the ideal coating design [87].

1.8. Problem of Study

The ocean comprises 70% of the earth's surface and facilitates 90% of global trade transportation. Due to this, the marine industry and resources have become a crucial aspect of economic development. The marine environment is a challenging and corrosive environment for materials used in the ocean industry. Seawater is a highly corrosive electrolyte. The primary cause of destruction and abandonment of infrastructure and industrial equipment in the marine environment is corrosion of materials. It is widely acknowledged globally that corrosion causes more losses than any other natural disaster [88] [89].

1.9. Research Objective

The objective of the proposed study lies in its examination of the effect of hydrophobic nanofillers on the corrosion protection effectiveness of epoxy coatings applied to Aluminum Alloy (AA-2219) substrate, specifically within the demanding marine environment. Assess the effect of these improved characteristics on the coating's capability to resist water, moisture, and saltwater, commonly found in marine settings. By exploring this uncharted territory, the research hopes to offer insightful contributions that can improve the toughness and longevity of protective coatings, advancing the understanding and application of materials for efficient corrosion mitigation in crucial marine applications.

Chapter 2

2. Experimental Section

2.1. Chemicals & Reagents

For the synthesis of materials, the employment of superior-grade synthetic ingredients and solvents was assured to attain purity in the end result. Cobalt nitrate hexahydrate, 2-methyl imidazole, epoxy (5052), hardener (5052), Tetraethyl orthosilicate (TEOS), and Tetrahydrofuran (THF) were acquired from Sigma Aldrich (Germany) and employed without any additional purification. Deionized water utilized in the preparation of electrolytes was taken from the deionizer set in the laboratory. 99% pure hydrochloric acid was obtained from BDH. Methanol and ethanol, both of which were acquired from Sigma Aldrich, were the solvents used in the synthesis of the nanoparticles.

2.2. Pretreatment of substrate

High strength aluminum alloy AA2219 is used as coating substrates. Aluminum alloys are extensively used for marine applications. The alloys were first cut into 1×1 cm^2 sheets, abraded with 1000 grit emery paper, washed with deionized water, and then ultrasonically degreased with acetone. The Aluminum alloys were then submerged in 0.5M HCl solution to remove the oxide layers from the surface. Finally, the substrates were washed with deionized water and then dried under a vacuum [90].

Figure 2:1: Substrate after pretreatment [91]

2.3. Preparation of ZIF-67

Dissolve 2.32g cobalt nitrate in 40 mL of methanol.2.46g 2-methyl imidazole was also dissolved in 40 mL methanol in another beaker. Sonicate both beakers separately for 40 minutes. Now mix both solutions. When 2-methyl imidazole is added to the cobalt nitrate solution, it turns purple and is sonicated for 2 hours to produce a homogeneous composition. After 24 hours, the final product was centrifuged, washed with methanol three times, and dried at 70^0C for three hours [92]. Procedure for synthesizing ZIF-67 is shown in Figure 2.2 and 2.3.

Figure 2:2: Procedure for synthesizing ZIF-67 [93]

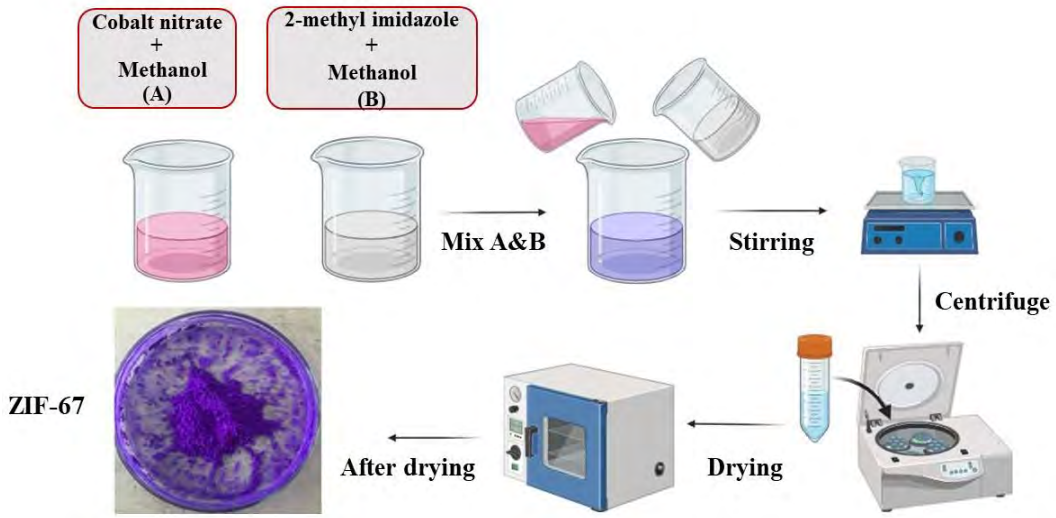

Figure 2:3: synthesis of ZIF-67

2.4. Preparation of ZIF-67@TEOS composite

In the preceding step, a quantity of 0.5 grams of ZIF-67 powder was produced, followed by the addition of 1 milliliter of TEOS to the beaker. The resulting mixture was vigorously stirred for a duration of 3 hours. The mixture was agitated for a duration of three hours. Subsequently, the sample underwent centrifugation at a velocity of 4000 revolutions per minute, and was consequently subjected to washing with ethanol. Following this, the ZIF-67@TEOS powder was obtained after undergoing a process of drying [94]. Procedure for synthesizing ZIF-67@ TEOS is shown in figure 2.4.

Figure 2:4: Procedure for synthesizing ZIF-67@TEOS

2.5. Preparation steps of coating

First, we coat the pure epoxy on the bare aluminum alloy (AA-2219). For this process, prepare 5g resin which have 3.6g epoxy and 1.4g hardener. Take 17.5ml THF (tetrahydrofuran) in beaker add epoxy into the beaker and sonicate for 40 minutes. After 40 minutes add hardener and again sonicate. After sonication a mixture was obtained and then coat the samples through dip coating and then dried. The ZIF-67@TEOS, which had already been prepared, were blended with epoxy resin at mass fractions of 6w% and 10w%. The particles were subsequently agitated and evenly distributed via ultrasound for a duration of 40 minutes in order to generate a homogeneous dispersion system. Subsequently, they were applied onto the aluminum alloy through dip coating. Coating procedure is shown in figure 2.5.

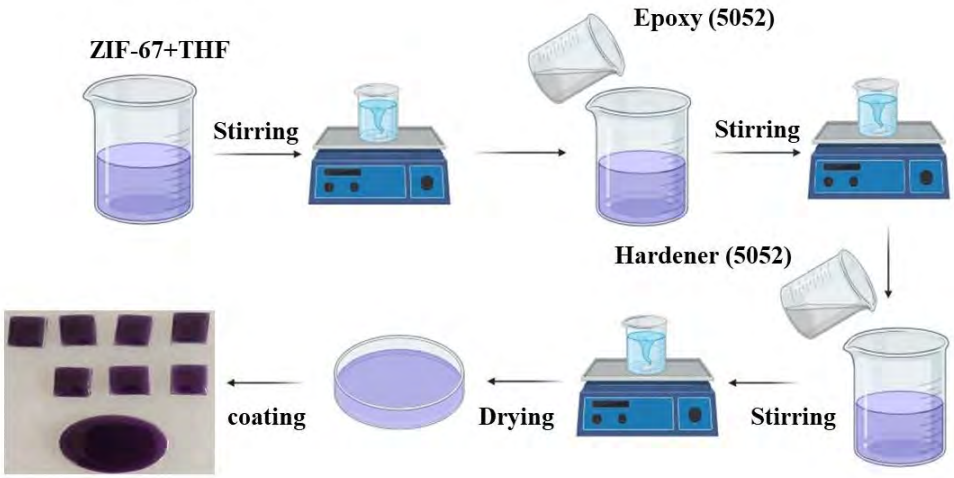

Figure 2:5: Coating procedures

2.6. Characterizations

2.6.1. X-ray diffraction (XRD)

The crystal structure and properties of materials are extensively studied using X-ray diffraction (XRD), a potent analytical technique. The basic idea behind this methodology is that when crystalline materials are exposed to X-rays, the interactions with the crystal lattice that result cause diffraction, which causes a specific diffraction pattern to emerge. The precise arrangement of atoms within a specific crystal can be determined using the diffraction pattern described here. This provides important information about the material's overall composition, crystallographic structure, and phase purity [95].

2.6.1.1. Working principle

X-ray diffraction relies on the constructive interference of monochromatic X-rays and a crystal sample. X-rays are produced by a cathode ray tube and filtered to create monochromatic radiation. The radiation is concentrated and aimed at the sample.

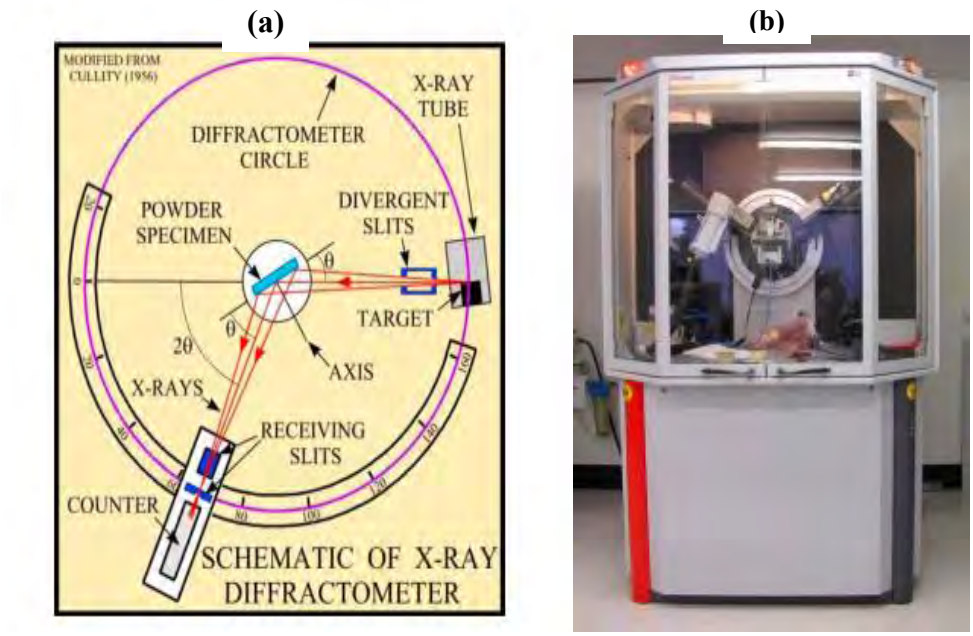

Figure 2:6: X-RAY Diffractometer (a) Schematic diagram (b) Tutorial view

2.6.1.2. Bragg's Law

A fundamental rule in X-ray crystallography known as Bragg's Law connects the angles of X-ray incidence and diffraction to the distance between crystal lattice planes and the wavelength of the X-rays. It is named after father-and-son team William Henry and William Lawrence Bragg. Mathematically, Bragg's Law can be stated as follows.

$$n\lambda = 2d \sin\theta$$

In the following equation,

- n is an integer that denotes the diffraction peak's order.

- The incident X-ray radiation's wavelength is λ

- d is the spacing between the crystal lattice planes.

- θ is the angle of the X-ray beam to the crystal lattice.

X-rays and crystals combine to produce a unique pattern called diffraction, which is explained by Bragg's Law. To achieve constructive interference, X-ray path difference needs to be a multiple of wavelength.

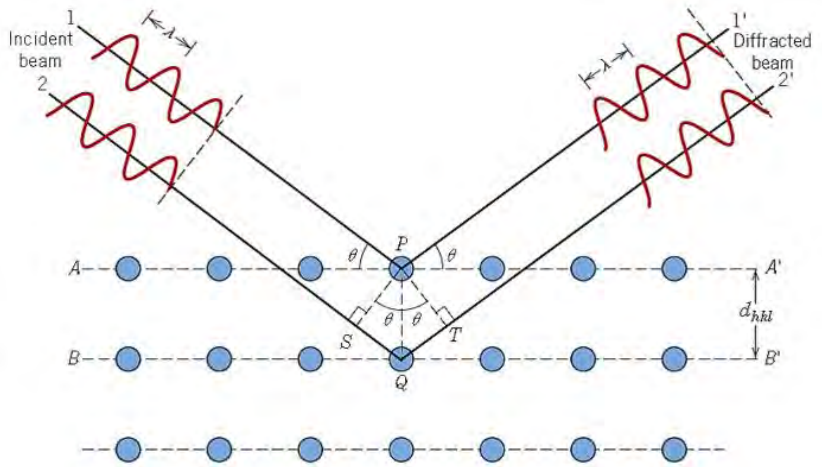

Figure 2:7: Bragg's crystal planes

Scientists utilize Bragg's Law to gauge the spacing of crystal lattice planes via analyzing diffraction angles and X-ray wavelengths. The comprehension of atom arrangement and crystal structure is crucial. Scientists can now uncover the mysteries of minerals and metals through structural analysis. X-ray crystallography has revolutionized science by revealing molecular structures and propelling fields like chemistry, materials science, and structural biology forward [96].

2.6.1.3. The Scherrer equation

The Scherrer equation is frequently applied in X-ray diffraction (XRD) to determine the average crystallite size of a substance based on the broadening of XRD peaks. Paul Scherrer, a German physicist, created the equation in 1918, and he is honored by having his name put on it. The Scherrer equation is presented as follows:

$$D = K\lambda / (\beta \cos \theta),$$

where:

- D is the average crystallite size,

- K is the Scherrer constant (typically taken as 0.9),

- λ is the X-ray wavelength,

- β is the full width at half maximum (FWHM),

- θ is the Bragg angle (in radians).

The Scherrer equation connects a material's crystallite size to the XRD peak broadening brought on by the finite size of the crystalline domains. In contrast to other elements like strain or lattice flaws, it is assumed that the peak broadening is primarily caused by the size of the crystallites. To apply the Scherrer equation, you need to measure the FWHM of a suitable XRD peak from the material of interest and know the X-ray wavelength used in the experiment. The Bragg angle, θ, can be calculated from the peak position using Bragg's law. You can use the Scherrer equation to determine the average crystallite size of the substance once you have the FWHM, X-ray wavelength, and Bragg angle. The Scherrer equation, it should be noted, assumes a uniform distribution of crystallite sizes and provides an average size estimation. The technique should be used carefully with other methods to understand the material's structure due to assumptions and simplifications.

2.6.1.4. Applications of XRD

To determine the development of a specific material system. To investigate the structure of the unit cell, including lattice parameters and miller indices.

Determine the nature of the phases within the substance. The present study aims to estimate the content of both crystalline and amorphous components present in the given sample. To determine the average crystallite size, strain, or micro-strain effects in bulk materials and thin film. To investigate the distortions in structure and temperature.

2.6.2. Scanning Electron Microscopy (SEM)

SEM is a method that employs an electron beam to create detailed images of a sample's surface. The data on the sample's topography, morphology, and composition is highly valuable. SEM is widely employed in various research and industrial sectors owing to its

proficiency in examining intricate details and analyzing the constituent makeup of substances.

2.6.2.1. Working Principle

The generation of a precise electron beam is utilized by the Scanning Electron Microscope in order to scan the surface of a given sample. When the beam interacts with the specimen, it generates signals comprising of secondary and backscattered electrons. Signals are detected and employed to produce superior images that disclose extensive information about the characteristics, organization, and composition of the sample's surface.

2.6.2.2. Components of Scanning Electron Microscope

A Scanning Electron Microscope (SEM) generates accurate images of sample surfaces using different components. The main elements of a scanning electron microscope consist of...

i. **Electron Gun:** This unit creates a focused electron beam to interact with the material being examined. An apparatus emits electrons from a heated filament or field emission source.
ii. **Electron Optics:** The system for electron optics uses lenses and apertures to direct and concentrate the electron beam onto the sample. By its power, the beam is molded and aimed with precision.
iii. **Sample Stage:** The specimen is held on the sample stage with accurate placement and motion in x, y, and z directions. The instrument should be steady and flexible enough to handle various sizes and shapes of samples.
iv. **Vacuum System:** SEM works in a vacuum to avoid electron scattering and air molecule interaction. The microscope chamber is kept in a low-pressure environment by the vacuum system.
v. **Scanning Coils:** The coiling mechanism scans electrons on a sample surface in a pattern. The scanning coils quickly move the electromagnetic beam.
vi. **Detectors:** SEM uses different detectors to capture signals produced when the electron beam interacts with the sample. Everhart-Thornley detectors detect secondary electrons, while solid-state detectors detect backscattered electrons.

vii. **Imaging System:** The detectors send signals which turn into images on a monitor through electrical processing. The software might have more functions like zooming and enhancing contrast.

viii. **Control and Data Acquisition:** The SEM can be controlled by a panel or computer interface. Adjusting parameters is possible, including beam intensity, focus, and imaging mode. Data acquisition systems facilitate the retention and interpretation of obtained images and data.

ix. **Additional Accessories:** SEMs have the potential to expand their abilities using a variety of enhancements.

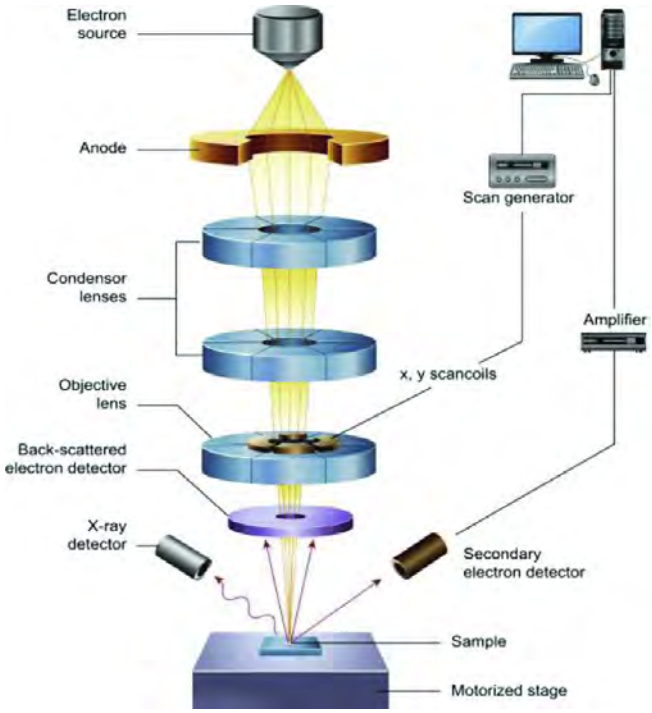

Figure 2:8: Schematic SEM

Advanced tools like EDS detectors, EBSD systems, and specimen holders can be used for elemental analysis, crystallographic information, and experiments under specific conditions.

A collaborative system that offers extensive imaging and analysis options, enabling researchers to examine samples with exceptional precision and detail. By utilizing a

Scanning Electron Microscope (SEM), one can extract numerous significant findings and data about the subject being studied. Some of the pivotal observations comprise:

- **Surface Topography**: SEM reveals intricate details of surface topography, enabling researchers to scrutinize surface characteristics such as roughness, texture, cracks, and irregularities. The comprehension of material structure depends on this vital information.
- **Morphology and Structure:** The SEM displays the sample's details at high magnification. This information includes observations of particle size, shape, orientation, and arrangement. To understand the characteristics and behavior of substances and to analyze their minute structure, knowledge is essential.
- **Elemental Composition:** To examine sample composition, SEM and EDS can collaborate. The elements that are present and their concentrations are revealed by EDS by the X-rays that the sample emits when struck by electrons.
- **Chemical Mapping:** By scanning the sample surface with an electron beam and analyzing the X-rays that are emitted, SEM with the aid of EDS can create maps of the elements. Scientists can investigate chemical changes and identify compositional shifts thanks to the maps, which show the pattern and density of the sample's constituents.
- **Phase Identification:** Phases or components in a sample can be identified using SEM. Researchers can distinguish between various materials in a sample and determine their proportions by looking at backscattered electrons, or EDS.
- **Defect Analysis:** Materials flaws like cracks, voids, grain boundaries, and dislocations can be found using SEM. The value of this information is found in assessing material quality, understanding breakdown processes, and improving production methods.
- **Biological Studies:** For examining the outside structure of cells, tissues, and microorganisms, SEM is a frequently used tool in biology. Researchers can investigate the characteristics of biological specimens' surfaces, including their behavior and the shape of cells.

The surface, morphology, structure, and composition of various materials are all thoroughly uncovered by the researchers can make sense of their characteristics, behaviors, and output.

2.6.3. Fourier Transform Infrared Spectroscopy (FTIR)

FTIR is a valuable analytical approach for determining and evaluating the chemical make-up of diverse materials. Each molecule has a specific "fingerprint" that may be used to distinguish and define it based on how it absorbs and emits infrared light. Scientists may investigate the content and structure of varied materials, such as liquids, solids, and gases, using FTIR spectroscopy, which measures the intensity of infrared light before and after it interacts with a sample. FTIR is a significant tool in a range of sectors because to its versatility and non-destructiveness [97].

2.6.3.1. Working Principle

The FTIR studies the sample's emission and absorption of infrared light. According to one concept, chemical bonds vibrate at precise frequencies when exposed to infrared light.

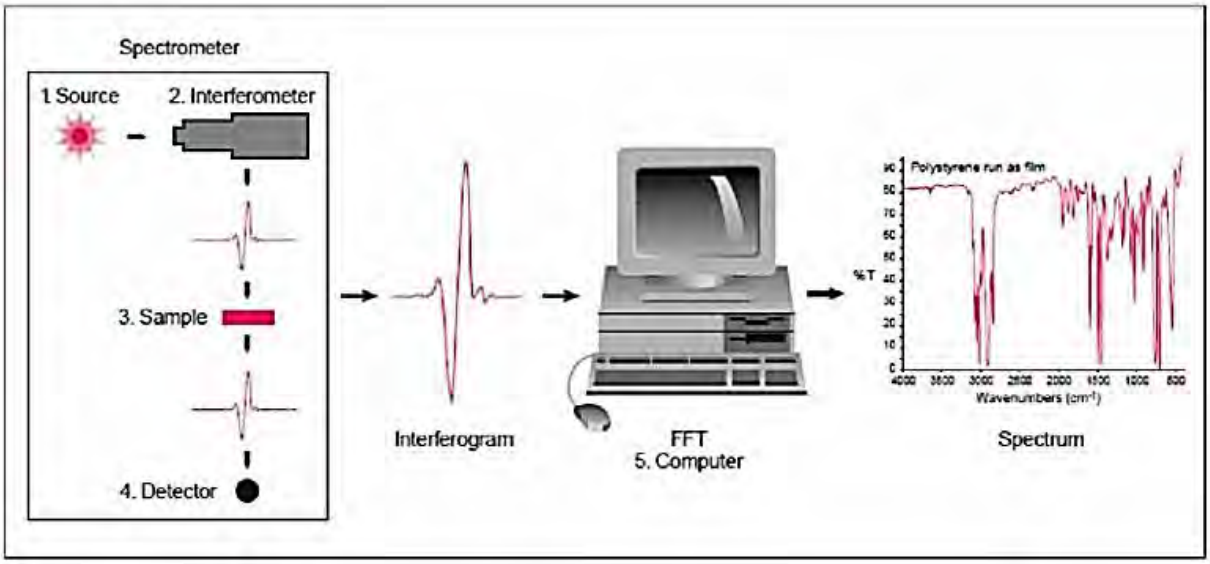

Figure 2:9: FTIR working principle

In FTIR spectroscopy, a wide range of infrared light passes through the material. The sample absorbs particular infrared light wavelengths that are consistent with the vibrations of its molecules. Light that is still present is captured by the detector. Light is split into

sample and reference beams for FTIR spectroscopy using an interferometer. Different interactions occur between the reference and sample beams. An interferogram with an interference pattern is produced by the recombined beams [98]. To obtain the interferogram, the intensity of the combined beams is time-domain measured. The interferogram is subjected to the exquisite Fourier Transform method in order to reveal the true spectrum. Interferogram time-domain becomes frequency-domain spectrum thanks to the Fourier Transform's magic. The resulting spectrum displays the sample's emission or absorption of infrared light at various frequencies. By comparing a sample's spectrum to reference spectra, scientists can determine the chemical bonds and functional groups in a sample's molecular structure.

FTIR spectroscopy reveals the chemical composition and molecular structure of various substances, aiding in precise analysis and identification of unknown materials.

2.6.3.2. Components of FTIR

- **Infrared Source**: Unleashes a vast spectrum of infrared rays.
- **Interferometer**: The incoming light is divided into two beams, creating interference patterns.
- **Sample Compartment**: Holds the sample for interaction with the infrared light.
- **Detector**: Analyzes the strength of light post-sample interaction.
- **Fourier Transform**: Transforms the interferogram to a spectrum in the frequency domain.
- **Data System**: Gathers, handles, and evaluates the spectral information.
- **Reference Library**: The reference spectra help to compare and identify sample components [99].

2.6.4. X-RAY Photoelectron Spectroscopy

A quantitative method for analyzing a material's surface's elemental composition, XPS also establishes the binding states of the elements [100]. It is a technique of surface analysis that is commonly employed to expose particulars regarding the empirical constitution, chemical configuration, and electronic configuration of the constituents encompassed

within a substance. Except for hydrogen, all of the surface elements present can be identified and quantified thanks to the energy and intensity of this peak [101].

2.6.4.1 Working Principle:

Einstein's photoelectric effect, in which electrons are emitted from atoms in response to electromagnetic radiation, is used in XPS. In the event that the energy of the photon incident exceeds that of the electron's binding energy, the electron shall be emitted [102]. The diverse binding energies of individual electrons and the presence of numerous orbitals at varying energy levels in atoms lead to the generation of multiple electrons with dissimilar binding energies, thereby creating an XPS spectrum.

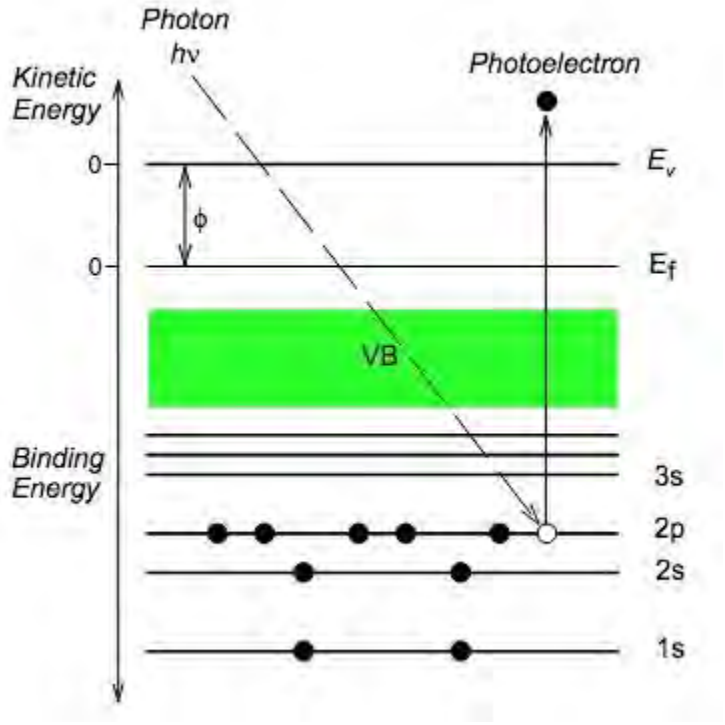

Figure 2:10: Sample energy diagram. [103]

2.6.4.2 XPS Spectrum:

Binding Energy (eV) is plotted on the X-axis versus time in XPS spectra. measured photoelectron counts on the Y axis. Usually, data are gathered in.

a) Survey mode to compile an exhaustive list of all the elements on a surface made of material, as in Figure 2(a).

b) High resolution scans of peaks of interest are also used to identify the chemical bonds connecting the target elements. Figure 2(b) shows a high resolution C1s spectrum as an example.

The photoelectrons of a surface sample are utilized as a distinguishing characteristic to discern the constituent elements by assessing their respective binding energies, thus serving as a unique "fingerprint." Chemical shifts in the X-ray photoelectron spectroscopy (XPS) spectra can be observed when an element transits into a novel bound state, and as a result, the binding energies of core electrons are modified. In general, the binding energy tends to augment with the increasing oxidation state, while it decreases with the addition of valence electrons [103].

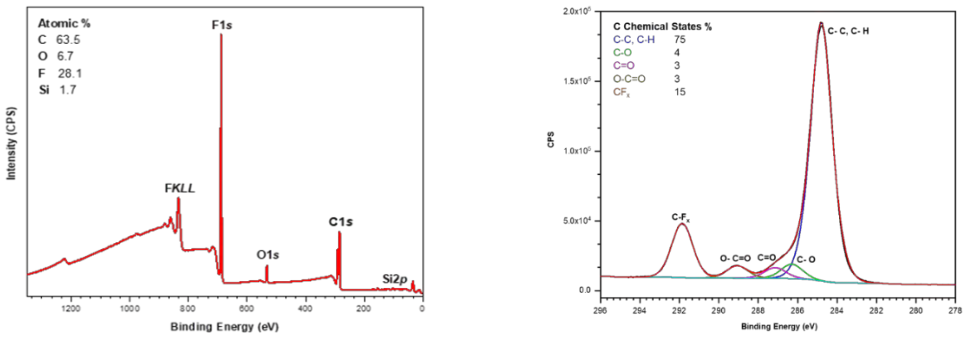

Figure 2:11: (a) example survey scan, (b) a high resolution C1s spectrum 86

2.6.5. Electrochemical Workstation

Gamry systems are widely utilized in electrochemistry for analyzing electrochemical cells, corrosion, battery materials and other related phenomena. Gamry setups provide various experimental techniques to examine diverse electrochemical processes including cyclic voltammetry (CV), Tafel, chronoamperometry, and electrochemical impedance spectroscopy (EIS), among others. Researchers in various disciplines, such as material

science, corrosion studies, energy storage, and sensor development, commonly utilize Gamry equipment to study and comprehend electrochemical behavior.

2.6.5.1. Components of Gamry setup

A Gamry setup is made up of several components.

i. **Potentiostat/Galvanostat:** This is the primary tool in Gamry's setup, with the ability to control voltage or current applied to the electrochemical cell under study. The potentiostat controls electrode potential and the galvanostat controls cell current. Potentiostats play a crucial role in electrochemistry research for understanding electrode processes, analytical chemistry, battery research, and ›n research.

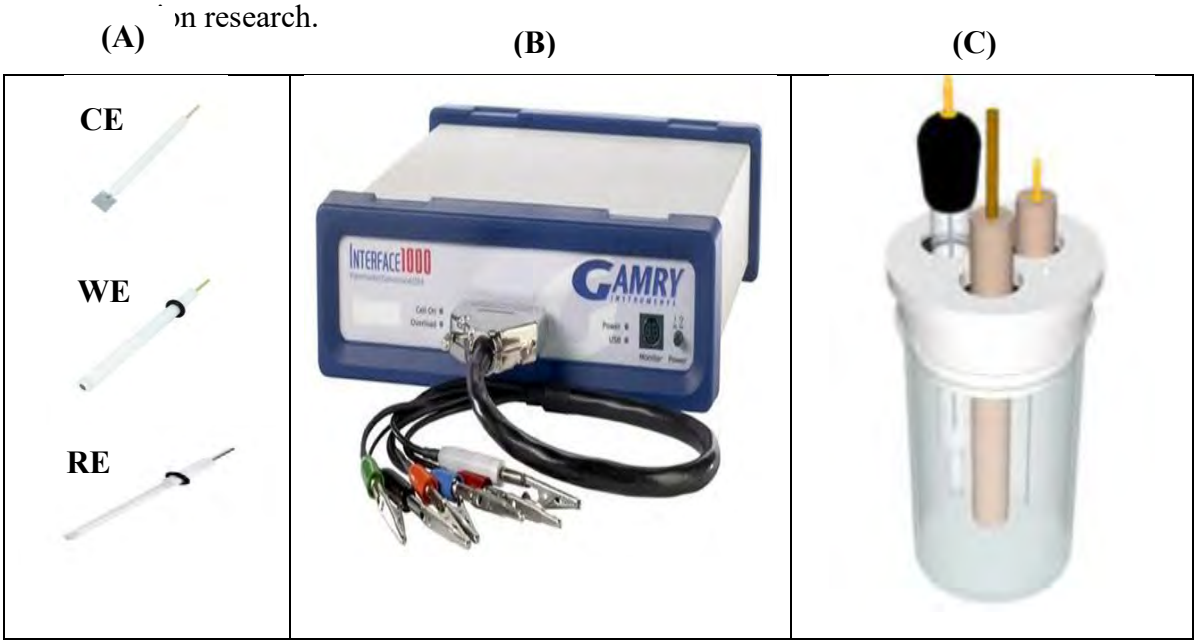

Figure 2:12: (A) Electrodes (B) Potentiostat/Galvanostat (C) Three-electrode system

ii. **Electrochemical cell:** The working electrode, reference electrode, and counter electrode are the three electrodes in an electrochemical cell. Electrochemical reactions can take place because these electrodes are in an electrolyte solution. Three electrodes are present in the electrochemical cell.

iii. **The working electrode (WE):** The desired reaction happens at the electrode's interface.

iv. **Counter electrode (CE):** The current flows between the working electrode and the counter-electrode.

v. **Reference electrode (RE):** An established and consistent potential exists for the reference electrode. It acts as the system's standard for regulating and gauging potential. It has a low current throughput. These electrodes are in an electrolyte solution to enable electrochemical reactions. The electrochemical process happens in the working electrode, the reference electrode provides a stable potential, and the counter electrode completes the circuit.

vi. **Computer and cell:** Gamry systems are linked to a computer with specific software from Gamry Instruments. This software permits users to operate the potentiostat/galvanostat, collect experimental data, and conduct data analysis.

vii. **Cables and Connectors:** Different cables and connectors are utilized to create electrical connections between the electrochemical cell and the potentiostat/galvanostat.

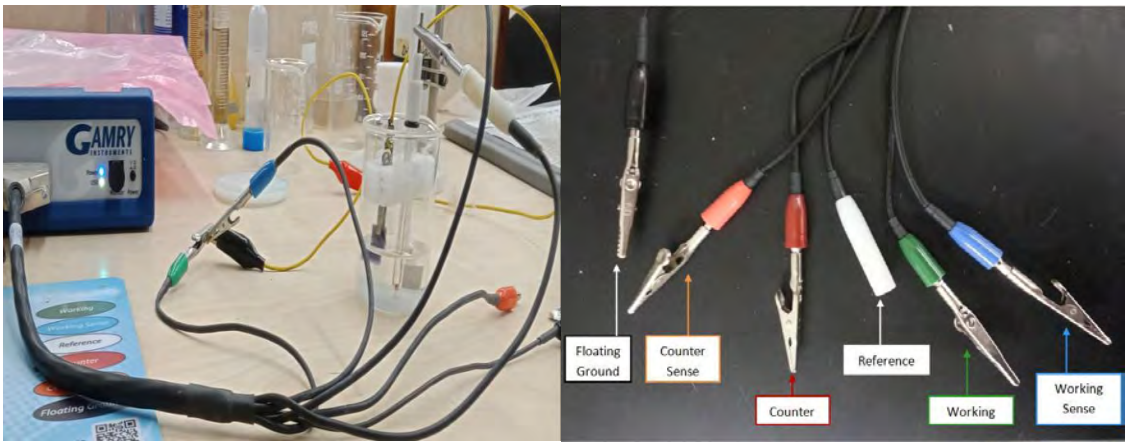

Figure 2:13: Cables and connectors for Gamry setup

2.6.5.2 Electrochemical Impedance Spectroscopy (EIS)

Electrochemical Impedance Spectroscopy (EIS) measures circuit impedance and has advantages over other electrochemical techniques. It is a steady-state and small signal analysis technique. Furthermore, it has the capability to investigate signal relaxations across a broad spectrum of frequencies with the aid of readily obtainable electrochemical

working stations [104]. EIS possesses the potential to explore various processes such as mass-transfer, charge-transfer, and diffusion. It has the ability to scrutinize intrinsic material properties or specific processes that could impact the conductance, resistance, or capacitance of an electrochemical system.

2.6.5.2 Representations of EIS

The expression for impedance is separated into real and imaginary parts. The real part is represented on the X-axis and the imaginary part on the Y-axis when plotted a Nyquist plot is shown in Figure 2.14.

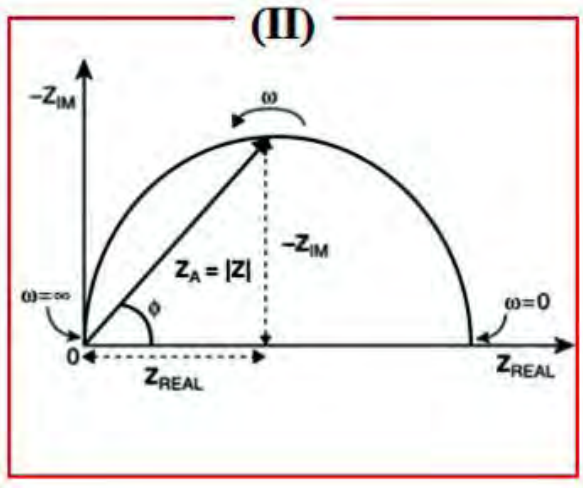

Figure 2:14: Nyquist plot with impedance vector

Every Nyquist plot point shows a negative Zimag at a certain frequency. Low frequencies conduct impedance on the right, while the left side shows high frequency generated impedances. The impedance representation on the plot is a vector of length |Z|. The angle between a vector and X-axis is known as "phase angle". Engineers prefer to use Bode plot to convey impedance results. Bode plot is composed of two logarithmic plots- magnitude vs frequency and phase vs frequency.

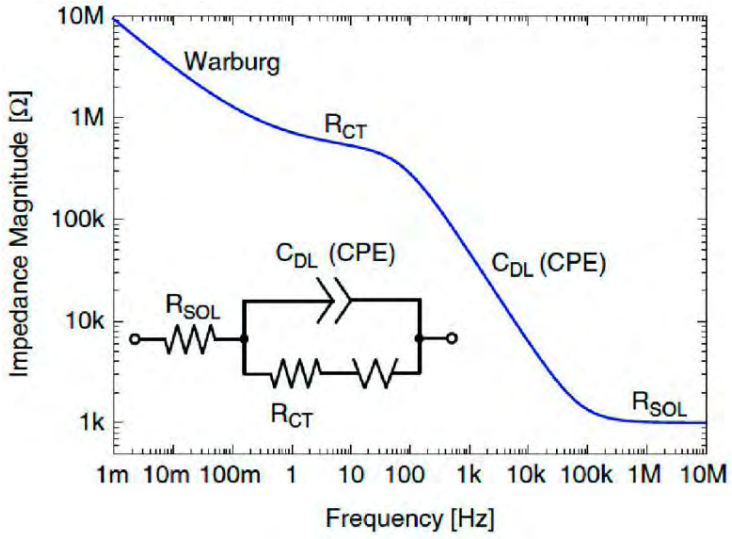

Figure 2:15: Bode plot

To gauge impedance, a prospective wave is utilized on the working electrode and the consequent current wave is noted. Two waves are observed to get Z, Φ, Zreal, and Zimag, and these are used to assess the range of potential waves with different frequencies. Electrochemical impedance spectroscopy was initially introduced in 1975 [105]. When a slight fluctuation in voltage occurs, the resulting current is measured [106] [107]. In a three-electrode configuration, EIS tests are done at a constant voltage. Nyquist plots demonstrate Rs, Rct, and W values. Faradaic and non-Faradaic are the two types of EIS. Faradaic EIS results from redox reactions, whereas non-Faradaic EIS is generated by double-layer capacitance. Faradaic current, which is used for accurate analysis, is the movement of electrons on electrodes [108]. A Bode plot can uncover electrochemical system capacitance. Scully and Silverman share additional Bode plot understanding [109]. Capacitance is evaluated through Bode plots, while resistive processes are analyzed with Nyquist plots [110]. The movement of molecules or redox species creates a resistance called Warburg impedance. This resistance changes with frequency, being small at high frequencies due to short diffusion distances. Warburg resistance is raised at low frequencies when redox molecules move easily. The Warburg effect appears as a diagonal line with a 45° slope on the Nyquist plot and causes a 45° phase shift on the Bode plot [111].

2.6.6. Polarization and Tafel

Polarization techniques involve Tafel extrapolation, potentiodynamic, cyclic and linear polarization. Tafel extrapolation plays a vital role in corrosion research. It is widely used and quicker than traditional methods. Tafel kinetics provide precise explanation of corrosion kinetics without considering mass transport limitations. Corrosion conditions are typically eliminated from reversible potentials of all reactions. When a metal is in water, reactions occur that corrode the metal. The reactions and potential are not equal [112].

The tafel plot showcases cathodic and anodic currents on a logarithmic scale. The corrosion potential (E_{corr}) is stabilized by this system. The upper curve represents cathodic current, while the lower curve represents anodic current. The tafel plot exhibits logarithmic cathodic and anodic currents. This system stabilizes the corrosion potential. The upper curve displays cathodic current, while the lower curve displays anodic current. The plotting along a logarithmic axis produces a sharp point. The logarithmic axis is required due to the wide range of current values in a corrosion experiment. The current can change significantly due to passivity during the experiment.

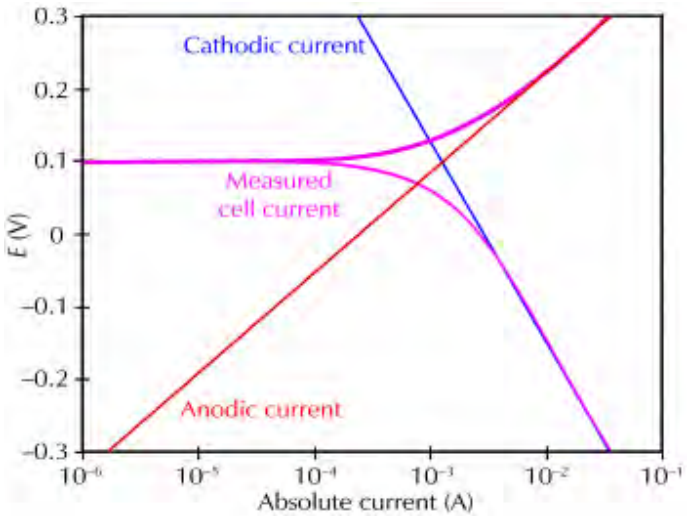

Figure 2:16: The corrosion process displays current's anodic and cathodic components.

The current in each half reaction is influenced by the electrochemical potential of the metal. Excessive electrons released during the anodic reaction will shift the metal's potential more

negative, leading to a slowdown in the anodic reaction and acceleration of the cathodic reaction. This adjustment counteracts the initial disruption of the system. The open-circuit potential or E_{oc} is the equilibrium potential of a metal without electrical connections. Measuring E_{oc} is the initial step in electrochemical corrosion experiments.

2.6.6.1 Quantitative Corrosion Theory:

Our corrosion process model is based on the assumption that the kinetics of the electron-transfer reaction at the metal surface governs the rates of the anodic and cathodic processes. This is typically true for reactions involving corrosion. Tafel equation 1, under kinetic control, is obeyed by an electrochemical reaction.

$$I= I_o\, e^{2.303\,(E-E_o)/\beta} \qquad \textbf{(a)}$$

In equation (a) I is the current resulting from the reaction, I_o is a reaction-dependent constant called the exchange current, E is the electrode potential, E_0 is the equilibrium potential (constant for a given reaction), β is the reaction's Tafel constant (constant for a given reaction, with units of volts/decade).

The Tafel equations for the anodic and cathodic reactions in a corrosion system can be combined to generate the Butler-Volmer equation

$$I= I_{corr}\,(e^{2.303\,(E-E_{corr})/\beta_a} - e^{-2.303(E-E_{corr})/\beta_c}) \qquad \textbf{(b)}$$

In equation (b) I is the measured current from the cell in amperes, I_{corr} is the corrosion current in amperes, E is the electrode potential, E_{corr} is the corrosion potential in volts, β_a is the anodic β Tafel constant in volts/decade, β_c is the cathodic β Tafel constant in volts/decade.

Corrosion rate is calculated by following formula

$$R= KW/AdT \qquad \textbf{(c)}$$

In equation (c) K is constant, W is total weight loss, T is time taken for the loss of metal, A is the surface area of the exposed metal and d is the metal density in g/cm^3.

Chapter 3

3. Results and Discussion

3.1. X-RAY Diffraction Analysis

Figure 3:1: XRD pattern of pure ZIF-67

The X-ray diffraction patterns of ZIF-67 are depicted in Figure 12. The distinct diffraction peaks that are visible in Figure 3.1 exhibit the distinctive properties of ZIF-67, which possesses a remarkable level of crystallinity and purity. The peaks are located at certain 2θ values which are in agreement with the findings of previous references [113] [114]. The values are 7.43° (011), 10.48° (002), 12.81° (112), 14.77° (022), 16.49° (013), 18.10° (222), 24.57° (233), and 26.76° (134). The peaks are distinct and obvious, indicating some degree of crystallinity. Furthermore, Scherrer's equation [115] is used to calculate the average crystallite size of the ZIF-67 NPs. The average crystallite size is measured to be 0.0984 nm. It can be seen that the crystal behavior of ZIF-67 NPs is clearly affected by the presence of epoxy composite in the mixture, as shown in Figure 3.2. The amorphous phase of epoxy has been proven to be the reason of the broad peak seen at 2θ =19.50° [116] [117]. Figure 3.2(b) displays the XRD pattern of pure epoxy deposited on AA2219. This gives

AA2219 to present four crystalline peaks at around 38.27° (111), 44.24° (200), 64.9° (220), and 78.13° (311) [118], [119], along with the characteristic broad peak of epoxy at 2θ =19.50°. Furthermore, the pure ZIF-67 NPs' crystallographic peaks were retained in the ZIF-67+THF XRD pattern, as can be seen in Figure 3.2(c). This confirms that the THF addition in ZIF-67 did not affect the material's crystallinity and that the material exhibits resilience under this mixing.

Table 3:1: Structural parameters of ZIF-67

Sample Name	Peak position (2θ)	Hkl	FWHM (β)	Crystallite Size D (nm)	D nm (Average)
ZIF-67	7.43	11	81.542	0.1015	0.0984
	10.48	2	80.738	0.1022	
	12.81	112	90.256	0.0913	
	14.77	22	88.435	0.093	
	16.49	13	86.799	0.0945	
	18.1	222	85.163	0.0961	
	24.57	233	78.742	0.1029	
	26.76	134	76.115	0.106	

Figure 3:2: XRD pattern for (a) Pure Epoxy (b) ZIF-67+Epoxy (c) ZIF-67+THF

3.2. Fourier Transform Infrared Spectroscopy (FTIR)

Figure 3:3: FTIR of ZIF-67

The Fourier transform infrared (FTIR) spectra of ZIF-67 acquired, are presented in Figure 3.3. The prominent feature observed in the spectra is a sharp and well-defined absorption band located at a wavenumber of 423 cm^{-1}. This specific absorption band can be ascribed to the Co-N stretching vibration, which serves as a definitive indicator of the presence of a chemical bond between the cobalt (Co) ions and the nitrogen (N) atoms within the 2-methylimidazole ligands. Furthermore, an additional absorption band was identified at 693 cm^{-1}, and its origin is likely associated with the bending vibration of the 2-methylimidazole ring. This finding further supports the structural integrity and presence of the 2-methylimidazole ligand within the ZIF-67 framework [120]. The infrared spectra of ZIF-67 exhibited distinct bands at wavenumbers 755, 993, 1141, 1305, 1418, and 1582 cm^{-1}. Of particular significance, the specific signal observed at 1582 cm−1 is indicative of stretching modes associated with the presence of C=C and C=N bonds within the ZIF-67 structure. An additional discernible band emerged at 3135 cm^{-1}, and its assignment can be

attributed to the stretching mode of C−H functionalities originating from the aliphatic chain within the linker, 2-methylimidazole [121].

Figure 3:4: FTIR Spectrum of Pure Epoxy and ZIF-67+Epoxy

Table 3:2: Vibration bands of ZIF-67 using FTIR

Wavenumber (cm-1)	Bond
423	Co-N stretching vibration
693	C-H bending vibration
7,551,305	out-of-plane and in-plane bending
1418	stretching vibration of entire imidazole ring
993	bending vibration of C-N in the imidazole ring
1141	stretching vibration C-N in imidazole ring
1582	C=N stretching vibration

The pure epoxy sample shown in Figure 3.4(a) gives the absorption peaks at 2855 cm^{-1} and 2920 cm^{-1} corresponding to C–H stretching in epoxy. The symmetrical stretching or ring breathing frequency is also observed between 1000–1300 cm^{-1}, which corresponds to

the C–O stretches indicating the characteristic of the epoxy ring [122]. The addition of ZIF-67 into epoxy causes observable changes in the FTIR spectrum, as shown in Figure 3.4(b). Some peaks in pure ZIF-67 shift to both lower and higher wavenumbers, indicating potential interactions with the framework's functional groups. Lower wavenumber shifts may weaken the bond, while higher shifts may indicate strengthening or new bond formation. The FTIR spectrum of epoxy-modified ZIF-67 shows new bands at 2920, 2855, 1735, 1610, 1367, and 1236 cm^{-1} that correspond to the epoxy functional groups vibrational modes. These bands confirm the successful incorporation of epoxy into the ZIF-67 structure, in addition to peak shifts. Some peaks as shown in Fig.3.4 (b) (423,755,1141,1418) are the peaks of ZIF-67 that shows the existence of ZIF-67 in epoxy. It shows that ZIF-67 did not decompose in epoxy.

3.3. Scanning Electron Microscopy (SEM)

The morphology of pure ZIF-67, pure epoxy, and dispersed ZIF-67 on epoxy was observed by SEM, as shown in Figure 3.5(A) & 3.6(a-b), respectively. The ZIF-67 material's SEM picture, Figure 3.5(B), showed a uniform dodecahedral shape with identifiable characteristics. The dodecahedral particles exhibited a uniform size distribution, indicating a well-controlled synthesis process. Although some sections of the ZIF-67 material's surface showed minor imperfections and surface roughness, over all the surface looked to be quite smooth.

(A) **(B)**

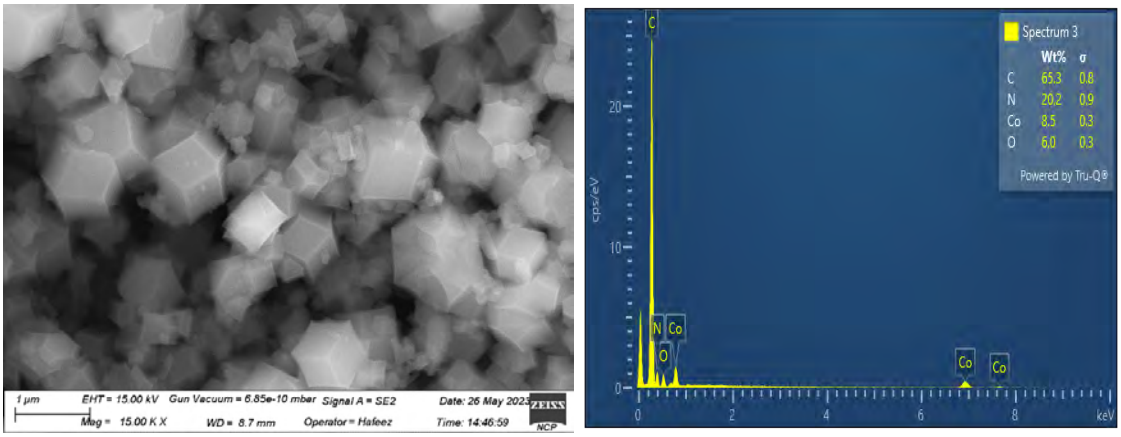

Figure 3:5: (A) SEM and (B) EDX of ZIF-67

It was easy to see the dodecahedral shape, which had sharp corners and edges. The particles had an average size of 310.85 nanometers, while their sizes ranged from 180 to 440 nanometers (see Figure 3.5). The ZIF-67 contained a number of elements, as shown by the EDX spectrum, in Figure 3.5(B), that was obtained after the analysis. The most prominent elements discovered are listed in Table 3.3 along with the corresponding atomic percentages.

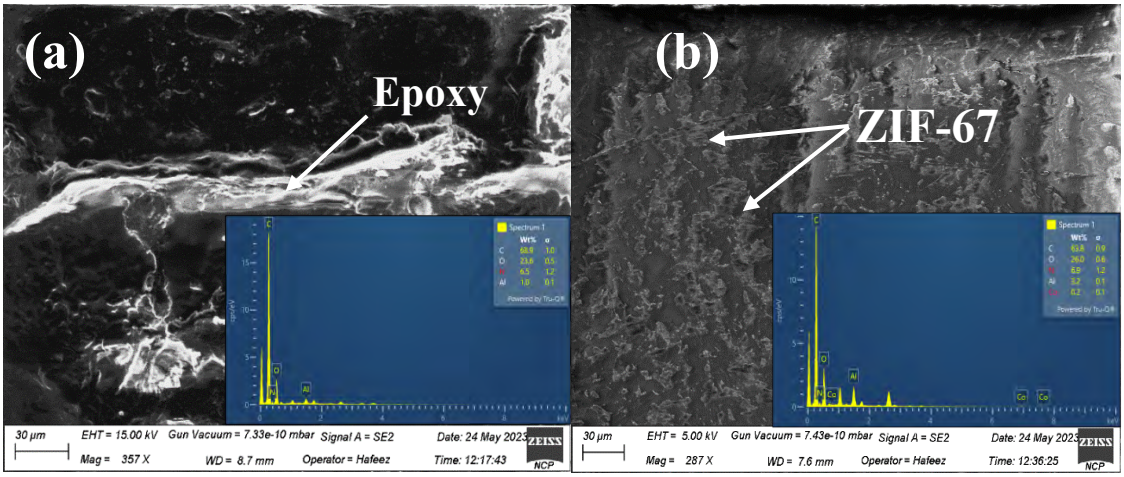

Figure 3:6: SEM of (a) Pure epoxy (b) Dispersed ZIF-67 on epoxy

Table 3:3: EDX of ZIF-67

Elements	Weight (%)	σ
C	65.3	0.8
N	10.2	0.9
Co	8.5	0.3
O	6.0	0.3

The SEM picture revealing the surface characteristics of pure epoxy is illustrated in Figure 3.6 (a). Generally, a smooth surface can be seen, though a significant difference is evident in the central region where a somewhat rugged fracture morphology is illustrated. This particular variation in surface topography highlights a shift from smoother areas to a marginally rougher texture, indicating the possible presence of discrepancies in either the mechanical properties or the manufacturing process within this specific region. The ZIF-67 (Zeolitic Imidazolate Framework-67) nanoparticles are shown dispersed within the matrix of pure epoxy in the SEM image that is being presented in Figure 3.6 (b). The image,

in particular, shows an approximately a uniform distribution of ZIF-67 nanoparticles over the epoxy substrate. Visually observable even dispersion confirms ZIF-67's successful fusion with the epoxy matrix. The image's two distinct features, which indicate the presence of ZIF-67 nanoparticles on the epoxy material's surface, are highlighted by arrows and are of particular interest. These arrows draw attention to how easily ZIF-67 nanoparticles interact with and adhere to the epoxy substrate, supporting both their effective dispersion and potential interfacial interaction.

Figure 3:7: SEM Particle size distribution

3.4.X-RAY Photoelectron Spectroscopy (XPS)

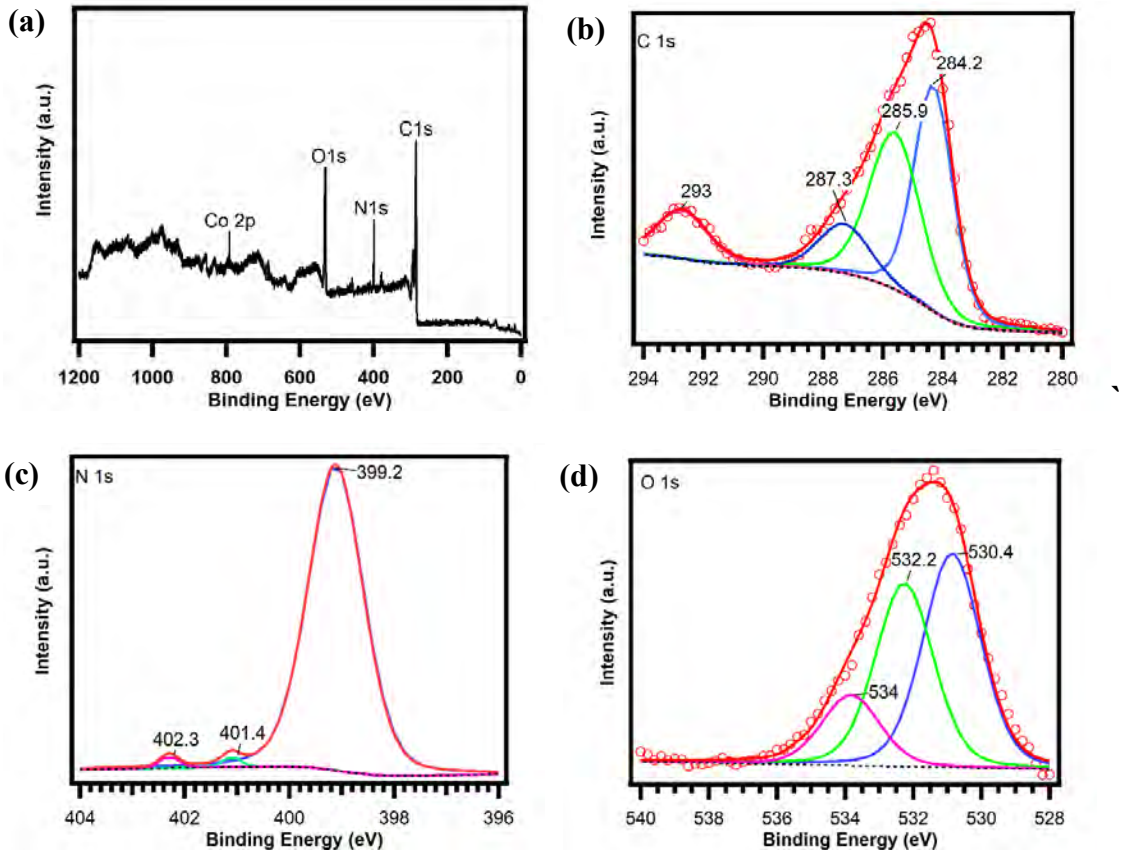

Figure 3:8: (a) wide survey spectra of ZIF-67, deconvoluted (b) C1s spectra, (c) N1s spectra, and (d) O1s spectra.

A comprehensive X-ray photoelectron spectroscopy (XPS) survey spectrum of ZIF-67 is depicted in Figure 3.8 (a). The spectrum predominantly exhibits peaks at binding energies of 284 eV (C1s), 399 eV (N1s), 532 eV (O1s), and 791 eV (Co 2p), which provide further evidence for the successful formation of ZIF-67. The C1s spectrum, depicted in Figure 3.8 (b), exhibits a refined decomposition into four discernible peaks. These peaks include C–C at 284.2 eV, C–O/C–N at 285.9 eV, C= O/C= N at 287.3 eV, and π-π* transitions at 293.0 eV. Figure 3.8 (c) presents the high-resolution N 1s spectrum and its deconvolution outcomes. Notably, aside from the intricate 2-methylimidazole peak observed at 399.2 eV for C=N, the peaks situated at 401.4 and 402.3 eV corresponded with the nitrogen atoms present on the imidazole rings [123]. Figure 3.8 (d) depicts the core level spectrum of O1s,

which manifests three distinct peaks at 530.4 eV, 532.2 eV, and 534.0 eV. These peaks correspond to the metal oxygen bond, oxygen originating from adsorptive water, and chemisorbed oxygen, respectively [124]. This XPS analysis gives good insights into the material's surface chemistry and possible applications.

3.5. Electrochemical Impedance Spectroscopy (EIS)

Electrochemical measurements were performed using Gamry potentiostat/galvanostat in the frequency range of 10^6 to 10^{-1} Hz with an AC amplitude of 10 mV. Bare aluminum alloy (AA-2219) and coated samples were used as working electrodes with exposed area of 1cm^2 Ag/AgCl and platinum sheet as reference and counter electrode respectively.

(a) **(b)**

Figure 3:9: Nyquist plots (a) and bar graph (b) of Bare Aluminum alloy (AA-2219) (B) pure epoxy (PE) ZIF-67+epoxy (ZE) (6wt%) ZIF-67@TEOS+epoxy (ZTE-I) and (10wt%) ZIF-67@TEOS+epoxy (ZTE-II) variants of different coated samples after different time intervals of immersion in 3M NaCl solution.

Anti-corrosion performance of bare aluminum alloy, Pure epoxy, ZIF-67+epoxy, ZIF-67@TEOS+Epoxy (6w%) and ZIF-67@TEOS+Epoxy (10w%) was estimated using EIS measurements. After one week and two weeks of immersion in a 3M NaCl solution, the Nyquist plots of five samples are shown in Fig.3.9. The impedance arc's size has a direct relationship with the coating's corrosion resistance; the more significant the impedance arc, the higher the corrosion resistance. The Nyquist plots of coated samples in Fig.3.9(a) shows that the bare aluminum alloy (AA-2219) has the lowest impedance arc. While the (6w%) ZIF-67@TEOS+epoxy coating has the largest impedance arc. The employment of TEOS facilitates effective bonding between the organic and inorganic phases, thereby preventing phase separation. ZIF-67 has a high surface area and adjustable pore size that provides

channels to TEOS which is a cross-linking agent that increases corrosion resistance. The use of ZIF-67 hastens the process of curing reaction in epoxy that increases the corrosion resistance of the epoxy. It can also be shown from Fig.3.9(b) that the ZIF-67@TEOS+ Epoxy (6w%) has the highest corrosion resistance. The EIS parameters were achieved as shown in Table.3.4 and 3.5 by employing the Reap2cpe (equivalent circuit model) by using Echem analyst as shown in Fig.3.10.

Sample ID:

Blank	B
Pure epoxy	PE
ZIF-67+epoxy	ZE
(6wt%) ZIF-67@TEOS+epoxy	ZTE-I
(10wt%) ZIF-67@TEOS+epoxy	ZTE-II

Table 3:4: EIS parameters 0f Bare Aluminum alloy (AA-2219) and variants of different coated samples after one week of immersion in 3M NaCl solution.

Sample	**R_{soln} (ohms)**	**R_{cor} (ohms)**	**R_{po} (ohms)**	**C_{cor} (S*s^a) × 10^{-3}**	**n**	**C_c (S*s^a) × 10^{-4}**	**m**	**Goodness of Fit × 10^{-4}**
B	8.896	68.52	35.03	26.9	0.793	0.978	0.871	4.429
PE	7.663	409.1	4606	5.039	1	0.366	0.813	7.206
ZE	0.0796	10,120	808.4	1.950	0.638	2.753	0.2911	11.53
ZTE-I	14.96	10,130	881.1	0.01142	1	0.7339	0.7674	19.19
ZTE-II	8.265	172.0	78.18	13.03	0.595	2.397	0.6347	0.5391

Table 3:5: EIS parameters 0f Bare Aluminum alloy (AA-2219) and variants of different coated samples after Two weeks of immersion in 3M NaCl solution.

Sample	**R_{soln} (ohms)**	**R_{cor} (ohms)**	**R_{po} (ohms)**	**Ccor (S*s^a) × 10^{-5}**	**n**	**C_c (S*s^a) × 10^{-5}**	**m**	**Goodness of Fit × 10^{-4}**
B	15.16	1827	32.24	1.386	0.9067	1.730	0.9303	52.70
PE	6.964	3090	84.06	19	0.153	3.51	0.812	6.03
ZE	20.73	0.474	620.7	233	0.983	8.14	0.774	22.2

ZTE-I	17.07	27780	23.71	9.750	0.788	5.385	0.7567	9.181
ZTE-II	7.639	4770	16.76	0.794	0.933	4.45	0.790	1.05

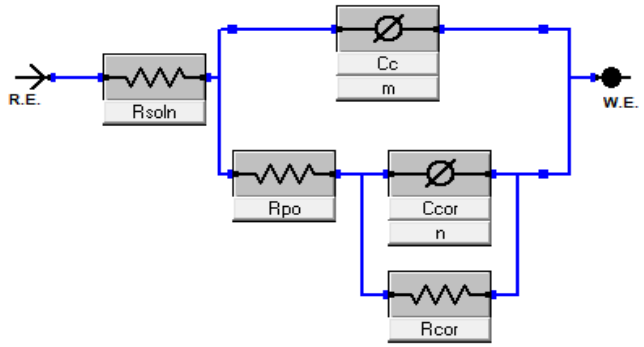

Figure 3:10: Reap2CPE circuit model for EIS data fitting

Table 3:6: EIS Parameters

R_{Soln} = Solution resistance	**m** = Exponent of coating capacitance
R_{Po} = Pore resistance	**C_c** = Coating capacitance
C_{Cor} = Corrosion capacitance	**W.E** = Working electrode
R_{Corr} = Corrosion resistance	**R.E** = Reference electrode
n = Exponent of double-layer capacitance	

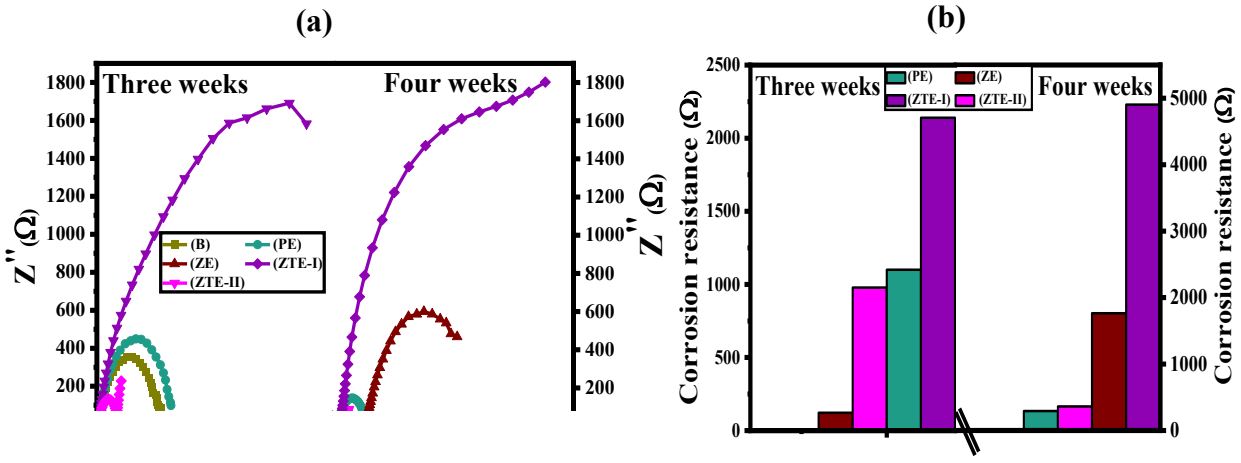

Figure 3:11: Nyquist plots (a) and bar graph (b) of Bare Aluminum alloy (AA-2219) (B) pure epoxy (PE) ZIF-67+epoxy (ZE) (6wt%) ZIF-67@TEOS+epoxy (ZTE-I) and (10wt%)

ZIF-67@TEOS+epoxy (ZTE-II) variants of different coated samples after different time intervals of immersion in 3M NaCl solution.

After three and four weeks of immersion in a 3M NaCl solution, the Nyquist plots of five samples are shown in Fig.3.11(a). The bare sample exhibits the lowest impedance arc when comparing the Nyquist plots of the different coated samples in Fig.3.11(a). In comparison to bare aluminum alloy, pure epoxy coating, and ZIF-67+ epoxy coating, the corrosion resistance of (6w%) ZIF-67@TEOS+epoxy is much greater, demonstrating that the small quantity 0f ZIF-67 and the addition of TEOS has significantly improved the corrosion resistance for epoxy coatings. It can also be shown from Fig.3.11(b) that the (6w%) ZIF-67@TEOS+epoxy has the highest corrosion resistance. EIS parameters were obtained after data fitting as shown in Table.3.7 and 3.8.

Table 3:7: EIS parameters 0f Bare Aluminum alloy (AA-2219) and variants of different coated samples after three weeks of immersion in 3M NaCl solution.

Sample	R_{soln} (ohms)	R_{cor} (ohms)	R_{po} (ohms)	C_{corr} (S*s^a) × 10^{-4}	n	C_c (S*s^a) × 10^{-5}	m	Goodness of Fit × 10^{-4}
B	9.161	6.711	1048	1.196	0.701	4.321	0.799	9.611
PE	12.82	1100	68.15	0.0145	0.989	2.70	0.815	15.7
ZE	20.51	121.6	49.17	0.155	0.951	133	0.254	6.20
ZTE-I	6.829	2140	2850	1.50	0.940	5.96	0.798	8.74
ZTE-II	7.394	978	299.4	66.1	0.100	6.59	0.896	9.91

Table 3:8: EIS parameters 0f Bare Aluminum alloy (AA-2219) and variants of different coated samples after four weeks of immersion in 3M NaCl solution.

Sample	R_{soln} (ohms)	R_{cor} (ohms)	R_{po} (ohms)	C_{cor} (S*s^a) × 10^{-5}	n	C_c (S*s^a) × 10^{-5}	m	Goodness of Fit × 10^{-4}
B	14.06	221.4	21.05	9.01	0.709	1.42	0.626	23.7
PE	8.592	293.3	347.2	685	0.174	2.62	0.815	5.32
ZE	337.8	1764	135.6	3.557	0.8159	3.666	0.579	2.279
ZTE-I	15.21	4903	22.58	10.93	0.808	6.966	0.7625	26.54
ZTE-II	14.76	361.4	76.20	942.6	0.712	27.56	0.724	8.702

Nyquist plots of Bare aluminum alloy (AA-2219) and different coated samples are shown in Fig.3.12(a) after two and three months of immersion in 3M NaCl solution. Pure epoxy and ZIF-67+Epoxy exhibit the lowest impedance arc in three months of time interval when comparing the Nyquist plots of the different coated samples in Fig.3.12(a), while the (6w%) ZIF-67@TEOS+epoxy has the largest impedance arc. This is due to the excellent dispersion of ZIF-67@TEOS in epoxy coatings, resulting in improved corrosion resistance of epoxy coatings. It can also be shown from Fig.3.12(b). that the ZIF-67@TEOS+ Epoxy (6w%) has the highest corrosion resistance. EIS parameters were obtained after data fitting as shown in Table.3.9 and 3.10.

(a) **(b)**

Figure 3:12 : Nyquist plots (a) and bar graph (b) of Bare Aluminum alloy (AA-2219) (B) pure epoxy (PE) ZIF-67+epoxy (ZE) (6wt%) ZIF-67@TEOS+epoxy (ZTE-I) and (10wt%) ZIF-67@TEOS+epoxy (ZTE-II) variants of different coated samples after different time intervals of immersion in 3M NaCl solution.

Table 3:9: EIS parameters 0f Bare Aluminum alloy (AA-2219) and variants of different coated samples after two months of immersion in 3M NaCl solution.

Sample	**R_{soln} (ohms)**	**R_{cor} (ohms) × 10^3**	**R_{po} (ohms)**	**C_{cor} (S*s^a) × 10^{-3}**	**n**	**C_c (S*s^a) × 10^{-6}**	**m**	**Goodness of Fit × 10^{-3}**
B	23.69	1.38	1510	2.60	1.00	155.	0.356	1.63
PE	16.982	2.65	49.71	0.0561	0.743	10.3	1.00	22.5
ZE	13.39	2.45	494.4	0.0714	0.565	6.91	0.519	7.61

ZTE-I	37.39	3.157	77.77	0.1488	0.7771	14.40	1.00	79.14
ZTE-II	18.74	0.970	39540	0877.2	0.7611	218.4	0.8559	9.767

Table 3:10: EIS parameters 0f Bare Aluminum alloy (AA-2219) and variants of different coated samples after three months of immersion in 3M NaCl solution.

Sample	**R_{soln} (ohms)**	**R_{cor} (ohms)**	**R_{po} (ohms)**	**C_{cor} (S*s^a) × 10^{-6}**	**n**	**C_c (S*s^a) × 10^{-5}**	**m**	**Goodness of Fit × 10^{-3}**
B	3.501	1940	772.7	181	0.924	10.7	0.769	3.20
PE	10.99	12.22	3.407	9.27	1	0.333	1	32.4
ZE	2.864	0.0286	4.542	0.087	0.973	1.04	1	160
ZTE-I	23.39	3297	183.7	57.36	0.8754	12.08	0.688	3.705
ZTE-II	63.87	647.4	344.9	3051	0.7	74.42	0.296	0.0825

Nyquist plots of Bare aluminum alloy (AA-2219) and different coated samples are shown in Fig.3.15 S1 after three months of immersion in 3M NaCl solution. ZIF-67+Epoxy exhibits the lowest impedance arc when comparing the Nyquist plots of the different coated samples in Fig.3.15 S1, while the ZIF-67@TEOS+ epoxy (6w%) has the largest impedance arc. This is due to the excellent dispersion of ZIF-67@TEOS in epoxy coatings, resulting in improved corrosion resistance of epoxy coatings. It can also be shown from Fig.3.15 S2. that the ZIF-67@TEOS+ Epoxy (6w%) has the highest corrosion resistance. EIS parameters were obtained after data fitting as shown in Table.3.10.

3.5. Tafel Polarization

In tafel plot potential is on y- axis while logarithm of current is on x-axis. The upper curve of the tafel plot is the cathodic current while lower curve is the anodic current. Sum of these two currents is corrosion current (I_{corr}). The tafel curves of the bare aluminum alloy (AA-2219) and different coated samples after one and two weeks of immersion in 3M NaCl solution are shown in Fig.3.13(a). Tafel parameters obtained after tafel fitting on curves such as $E_{corr,}$ $I_{corr,}$ and corrosion rate summarized in Table 3.11 and 3.12.

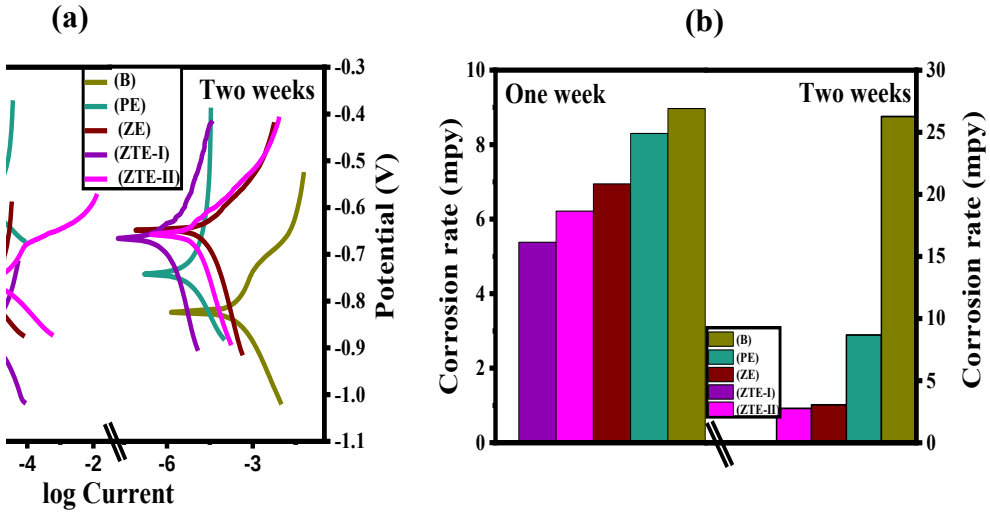

Figure 3:13: Tafel plots (a) and bar graph (b) of bare Aluminum alloy (AA-2219) (B) pure epoxy (PE) ZIF-67+epoxy (ZE) (6wt%) ZIF-67@TEOS+epoxy (ZTE-I) and (10wt%) ZIF-67@TEOS+epoxy (ZTE-II) variants of different coated samples after different time intervals of immersion in 3M NaCl solution.

Table 3:11: Tafel parameters 0f bare Aluminum alloy (AA-2219) and variants of different coated samples after one week of immersion in 3M NaCl solution.

Sample	β_a (V/decade)	β_c (V/decade)	I_{corr} (µA)	E_{corr} (mV)	Corrosion rate (mpy)
B	0.420	0.1	20.8	-869	8.969
PE	0.771	22.8	19.2	-468	8.299
ZE	0.629	26.2	16.1	-780	6.944
ZTE-I	0.5736	0.4342	24.90	-924	5.379
ZTE-II	0.253	16.4	28.8	-738	6.216

Table 3:12: Tafel parameters 0f bare Aluminum alloy (AA-2219) and variants of different coated samples after two weeks of immersion in 3M NaCl solution.

Sample	Beta A (V/decade)	Beta C (V/decade)	Icorr(µA)	Ecorr(mV)	Corrosion rate (mpy)
B	0.09	0.0669	122	-820	26.27
PE	0.803	0.245	20.1	-738	8.681
ZE	0.0552	0.122	14.2	-646	3.052
ZTE-I	0.0771	0.1057	0.541	-657	0.2334
ZTE-II	0.120	0.226	12.8	-646	2.768

After comparison of bare aluminum alloy and different coated samples it is observed that (6w%) ZIF-67@TEOS+epoxy has the best corrosion resistance performance. It can also be shown from Fig.3.13(b) that (6w%) ZIF-67@TEOS+epoxy has low corrosion rate.

I_{corr} = Corrosion current

E_{corr} = Corrosion potential

Beta A = Anodic Tafel slope

Beta C = Cathodic Tafel slope

The tafel curves of the bare aluminum alloy (AA-2219) and different coated samples after three and four weeks of immersion in 3M NaCl solution are shown in Fig.3.14(a). Tafel parameters obtained after tafel fitting on curves such as $E_{corr,}$ $I_{corr,}$ and corrosion rate summarized in Table 3.13 and 3.14. After comparison of bare aluminum alloy and different coated samples it is observed that (6w%) ZIF-67@TEOS+epoxy has the best corrosion resistance performance. It can also be shown from Fig.3.14 (b). and Table 3.15. that (6w%) ZIF-67@TEOS+epoxy has low corrosion rate.

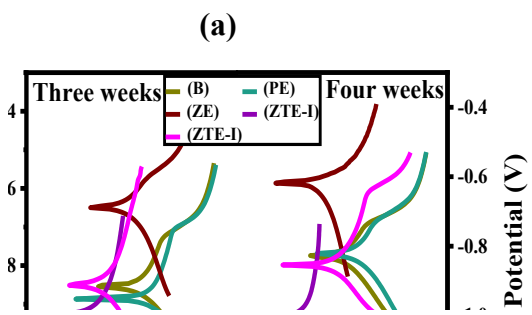

Figure 3:14: Tafel plots (a) and bar graph (b) of bare Aluminum alloy (AA-2219) (B) pure epoxy (PE) ZIF-67+epoxy (ZE) (6wt%) ZIF-67@TEOS+epoxy (ZTE-I) and (10wt%) ZIF-67@TEOS+epoxy (ZTE-II) variants of different coated samples after different time intervals of immersion in 3M NaCl solution.

Table 3:13: Tafel parameters 0f Bare Aluminum alloy (AA-2219) and variants of different coated samples after Three weeks of immersion in 3M NaCl solution.

Sample	Beta A (V/decade)	Beta C (V/decade)	Icorr(µA)	Ecorr(mV)	Corrosion rate (mpy)
B	0.139	0.0806	160	-851	34.47
PE	0.0839	0.0399	95.1	-883	20.51
ZE	0.176	0.184	141	-644	30.38
ZTE-I	0.713	0.498	29.6	-924	6.388
ZTE-II	0.533	0.326	46.5	-846	10.02

Table 3:14: Tafel parameters 0f Bare Aluminum alloy (AA-2219) and variants of different coated samples after four weeks of immersion in 3M NaCl solution.

Sample	Beta A (V/decade)	Beta C (V/decade)	Icorr(µA)	Ecorr(mV)	Corrosion rate (mpy)
B	0.143	0.130	156	-825	33.55
PE	0.231	0.146	489	-814	105.4
ZE	0.0658	0.258	17.3	-613	3.724
ZTE-I	0.6404	0.1162	7.860	-1000	3.390
ZTE-II	0.224	0.164	104	-851	22.44

The tafel plots of the blank and different coated samples after two and three months of immersion in 3M NaCl solution are shown in Fig.3.15(a). Tafel parameters obtained after tafel fitting on curves such as E_{corr}, I_{corr}, and corrosion rate summarized in Table 3.15 and 3.16. After comparison of bare aluminum alloy and different coated samples it is observed that (6w%) ZIF-67@TEOS+epoxy has the best corrosion resistance performance. It can also be shown from Fig.3.15(b) (6w%) ZIF-67@TEOS+epoxy has low corrosion rate.

(a) **(b)**

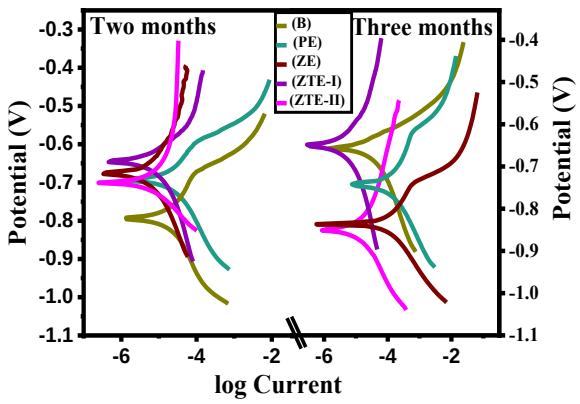

Figure 3:15: Tafel plots (a) and bar graph (b) of bare Aluminum alloy (AA-2219) (B) pure epoxy (PE) ZIF-67+epoxy (ZE) (6wt%) ZIF-67@TEOS+epoxy (ZTE-I) and (10wt%) ZIF-67@TEOS+epoxy (ZTE-II) variants of different coated samples after different time intervals of immersion in 3M NaCl solution.

Table 3:15: Tafel parameters 0f Bare Aluminum alloy (AA-2219) and variants of different coated samples after two months of immersion in 3M NaCl solution.

Sample	Beta A (V/decade)	Beta C (V/decade)	Icorr(µA)	Ecorr(mV)	Corrosion rate (mpy)
B	1.626	4.389	340	-790	73.33
PE	1.032	0.583	129	-689	27.85
ZE	0.9556	2.325	53.90	-676	11.62
ZTE-I	0.1421	0.1901	9.150	-645	3.947
ZTE-II	1.833	0.2448	25.70	-696	11.07

Table 3:16: Tafel parameters 0f Bare Aluminum alloy (AA-2219) and variants of different coated samples after three months of immersion in 3M NaCl solution.

Sample	Beta A (V/decade)	Beta C (V/decade)	Icorr(µA)	Ecorr(mV)	Corrosion rate (mpy)
B	0.0784	0.131	25.5	-652	5.497
PE	0.229	0.174	185	-743	39.9
ZE	0.141	0.117	128	-833	27.64
ZTE-I	0.3231	0.370	12.20	-650	5.251
ZTE-II	0.565	0.348	49.5	-846	10.67

Conclusion

The Pure ZIF-67 was synthesized successfully using solvothermal method. The material was analyzed both analytically and electrochemically. Fourier-transformed infrared spectroscopy (FT-IR) for functional group identification and to verify the formation of ZIF-67 nanoparticles. The peak at 423 cm^{-1} is associated with the Co-N stretching vibration that confirms the Co-N bond formation. Elemental identification and the relative abundance of the components on the surface of the material was carried through XPS. The spectrum predominantly exhibits peaks at binding energies of 284 eV (C1s), 399 eV (N1s), 532 eV (O1s), and 791 eV (Co 2p), which provide further evidence for the successful formation of ZIF-67. The structure and size of particles were studied with SEM, while EDX was used to observe the elemental composition. Average particle size was also calculated through SEM by using Image J which is 310.85 nm as reported. Aluminum Alloy (AA-2219), used in marine environment, was chosen as a substrate. Four types of superhydrophobic nano epoxy-based coatings, including Pure Epoxy, ZIF-67+Epoxy, (6w%) ZIF-67@TEOS+epoxy and (10w%) ZIF-67@TEOS+epoxy was applied using dip coating technique. The coatings were tested for corrosion protection using EIS and Tafel measurements to calculate the corrosion resistance (R_{corr}), pore resistance (R_{po}), solution resistance (R_{soln}), corrosion current (I_{corr}), corrosion potential (E_{corr}) and corrosion rate for a different time interval. Electrochemical studies revealed that (6w%) ZIF-67@TEOS+epoxy has a greater corrosion resistance which is 27,780 ohms for two weeks of immersion in 3M NaCl solution than the bare and different coated samples. (6w%) ZIF-67@TEOS+epoxy has greater corrosion resistance throughout the time interval from one week to three months. The corrosion rate, determined via tafel curve fitting, has demonstrated that (6w%) ZIF-67@TEOS+epoxy have displayed the lower corrosion rate for its application in the marine industry. The Tafel scan demonstrated a significant decrease in corrosion rate for (6w%) ZIF-67@TEOS+epoxy which is 0.2334 mpy for two weeks of immersion in 3M NaCl solution. This is because ZIF-67 possesses the ability to adsorb corrosive species due to their high surface area and adjustable pore sizes. ZIF-67-containing coatings have the ability to reduce the concentration of species at the metal surface, which slows down or prevents the corrosion process. It also accelerates the curing

reaction of epoxy which increases its corrosion protection performance. The employment of TEOS facilitates effective bonding between the organic and inorganic phases, thereby preventing phase separation. ZIF-67 has a high surface area and adjustable pore size that provides channels to TEOS which is a cross-linking agent that increases corrosion resistance. The results indicate that (6w%) ZIF-67@TEOS+epoxycoatings have better corrosion performance compared to bare aluminum alloy and different coated samples.

References

[1] G. K. Awari, V. S. Kumbhar, R. B. Tirpude, and S. W. Rajurkar, *Automotive manufacturing processes: A case study approach*. CRC Press, 2023. doi: 10.1201/9781003367321.

[2] D. N. Wang'ombe, "Development of Recycled Friendly Aluminium Alloys for Automotive and Structural Applications." JKUAT-COETEC, 2022.

[3] L. Ben Said, "The incremental sheet forming; technology, modeling and formability: A brief review," *Proc. Inst. Mech. Eng. Part E J. Process Mech. Eng.*, vol. 236, no. 6, pp. 2729–2755, 2022, doi: 10.1177/09544089221093306.

[4] C. Lin and Y. Yao, "Corrosion-Resistant Coating Based on High-Entropy Alloys," *Metals (Basel).*, vol. 13, no. 2, p. 205, 2023.

[5] P. S. Samuel Ratna Kumar, P. M. Mashinini, and R. Vaira Vignesh, "Overview of Lightweight Metallic Materials," in *Materials Horizons: From Nature to Nanomaterials*, Springer, 2023, pp. 75–87. doi: 10.1007/978-981-19-7146-4_4.

[6] M. Avateffazeli *et al.*, "On microstructure and work hardening behavior of laser powder bed fused Al-Cu-Mg-Ag-TiB2 and AlSi10Mg alloys," *Mater. Today Commun.*, vol. 35, p. 105804, 2023, doi: 10.1016/j.mtcomm.2023.105804.

[7] C. Lu *et al.*, "Radiation-induced segregation on defect clusters in single-phase concentrated solid-solution alloys," *Acta Mater.*, vol. 127, pp. 98–107, 2017, doi: 10.1016/j.actamat.2017.01.019.

[8] C. Cattò and F. Cappitelli, "Testing anti-biofilm polymeric surfaces: Where to start?," *Int. J. Mol. Sci.*, vol. 20, no. 15, p. 3794, 2019.

[9] P. J. Shull, *Nondestructive evaluation: theory, techniques, and applications*. CRC press, 2002.

[10] B. Abnar, S. Gashtiazar, and M. Javidani, "Friction Stir Welding of Non-Heat Treatable Al Alloys: Challenges and Improvements Opportunities," *Crystals*, vol. 13, no. 4, p. 576, 2023, doi: 10.3390/cryst13040576.

[11] A. Sharma and J.-P. Jung, "Aluminium Based Brazing Fillers for High Temperature Electronic Packaging Applications," *J. Microelectron. Packag. Soc.*, vol. 22, no. 4, pp. 1–5, 2015, doi: 10.6117/kmeps.2015.22.4.001.

[12] S. Kitagawa, "Metal–organic frameworks (MOFs)," *Chem. Soc. Rev.*, vol. 43, no. 16, pp. 5415–5418, 2014.

[13] D. Lan *et al.*, "Adsorptive removal of organic dyes via porous materials for wastewater treatment in recent decades: A review on species, mechanisms and perspectives," *Chemosphere*, vol. 293, p. 133464, 2022, doi: 10.1016/j.chemosphere.2021.133464.

[14] R. B. Choudhary, S. Ansari, and M. Majumder, "Recent advances on redox active composites of metal-organic framework and conducting polymers as

pseudocapacitor electrode material," *Renew. Sustain. Energy Rev.*, vol. 145, p. 110854, 2021, doi: 10.1016/j.rser.2021.110854.

[15] Y. He, B. Li, M. O'Keeffe, and B. Chen, "Multifunctional metal-organic frameworks constructed from meta-benzenedicarboxylate units," *Chem. Soc. Rev.*, vol. 43, no. 16, pp. 5618–5656, 2014, doi: 10.1039/c4cs00041b.

[16] N. L. Rosi *et al.*, "Hydrogen storage in microporous metal-organic frameworks," *Science (80-.).*, vol. 300, no. 5622, pp. 1127–1129, 2003, doi: 10.1126/science.1083440.

[17] Y. Cheng *et al.*, "Advanced Porous Materials in Mixed Matrix Membranes," *Adv. Mater.*, vol. 30, no. 47, p. 1802401, 2018, doi: 10.1002/adma.201802401.

[18] G. Cai, P. Yan, L. Zhang, H. C. Zhou, and H. L. Jiang, "Metal-Organic Framework-Based Hierarchically Porous Materials: Synthesis and Applications," *Chem. Rev.*, vol. 121, no. 20, pp. 12278–12326, 2021, doi: 10.1021/acs.chemrev.1c00243.

[19] M. D. Allendorf and V. Stavila, "Crystal engineering, structure–function relationships, and the future of metal–organic frameworks," *CrystEngComm*, vol. 17, no. 2, pp. 229–246, 2015.

[20] L. Pan *et al.*, "Metal-organic framework nanofilm for mechanically flexible information storage applications," *Adv. Funct. Mater.*, vol. 25, no. 18, pp. 2677–2685, 2015, doi: 10.1002/adfm.201500449.

[21] N. C. Burtch, H. Jasuja, and K. S. Walton, "Water stability and adsorption in metal-organic frameworks," *Chem. Rev.*, vol. 114, no. 20, pp. 10575–10612, 2014, doi: 10.1021/cr5002589.

[22] D. Shi, X. Yu, W. Fan, V. Wee, and D. Zhao, "Polycrystalline zeolite and metal-organic framework membranes for molecular separations," *Coord. Chem. Rev.*, vol. 437, p. 213794, 2021, doi: 10.1016/j.ccr.2021.213794.

[23] A. Phan, C. J. Doonan, F. J. Uribe-Romo, C. B. Knobler, M. Okeeffe, and O. M. Yaghi, "Synthesis, structure, and carbon dioxide capture properties of zeolitic imidazolate frameworks," *Acc. Chem. Res.*, vol. 43, no. 1, pp. 58–67, 2010, doi: 10.1021/ar900116g.

[24] Y. Arafat, M. R. Azhar, Y. Zhong, H. R. Abid, M. O. Tadé, and Z. Shao, "Advances in Zeolite Imidazolate Frameworks (ZIFs) Derived Bifunctional Oxygen Electrocatalysts and Their Application in Zinc–Air Batteries," *Adv. Energy Mater.*, vol. 11, no. 26, p. 2100514, 2021, doi: 10.1002/aenm.202100514.

[25] A. M. Mohamed, M. Ramadan, and N. K. Allam, "Recent advances on zeolitic imidazolate -67 metal-organic framework-derived electrode materials for electrochemical supercapacitors," *J. Energy Storage*, vol. 34, 2021, doi: 10.1016/j.est.2020.102195.

[26] A. M. Mohamed, A. O. Abo El Naga, T. Zaki, H. B. Hassan, and N. K. Allam, "Bimetallic Co-W-S Chalcogenides Confined in N,S-Codoped Porous Carbon

Matrix Derived from Metal-Organic Frameworks for Highly Stable Electrochemical Supercapacitors," *ACS Appl. Energy Mater.*, vol. 3, no. 8, pp. 8064–8074, 2020, doi: 10.1021/acsaem.0c01513.

[27] R. Chen *et al.*, "A two-dimensional zeolitic imidazolate framework with a cushion-shaped cavity for CO2 adsorption," *Chem. Commun.*, vol. 49, no. 82, pp. 9500–9502, 2013, doi: 10.1039/c3cc44342f.

[28] A. Phan, C. J. Doonan, F. J. Uribe-Romo, C. B. Knobler, M. Okeeffe, and O. M. Yaghi, "Synthesis, structure, and carbon dioxide capture properties of zeolitic imidazolate frameworks," *Acc. Chem. Res.*, vol. 43, no. 1, pp. 58–67, 2010, doi: 10.1021/ar900116g.

[29] C. Liu, M. Mullins, S. Hawkins, M. Kotaki, and H. J. Sue, "Epoxy Nanocomposites Containing Zeolitic Imidazolate Framework-8," *ACS Appl. Mater. Interfaces*, vol. 10, no. 1, pp. 1250–1257, 2018, doi: 10.1021/acsami.7b16711.

[30] S. Bibi, E. Pervaiz, and M. Ali, "Synthesis and applications of metal oxide derivatives of ZIF-67: a mini-review," *Chem. Pap.*, vol. 75, no. 6, pp. 2253–2275, 2021, doi: 10.1007/s11696-020-01473-y.

[31] M. Ramezanzadeh, B. Ramezanzadeh, M. Mahdavian, and G. Bahlakeh, "Development of metal-organic framework (MOF) decorated graphene oxide nanoplatforms for anti-corrosion epoxy coatings," *Carbon N. Y.*, vol. 161, pp. 231–251, 2020, doi: 10.1016/j.carbon.2020.01.082.

[32] O. Rodríguez-Uicab, J. L. Abot, and F. Avilés, "Electrical resistance sensing of epoxy curing using an embedded carbon nanotube yarn," *Sensors (Switzerland)*, vol. 20, no. 11, pp. 1–17, 2020, doi: 10.3390/s20113230.

[33] F. Awaja, M. Gilbert, G. Kelly, B. Fox, and P. J. Pigram, "Adhesion of polymers," *Prog. Polym. Sci.*, vol. 34, no. 9, pp. 948–968, 2009, doi: 10.1016/j.progpolymsci.2009.04.007.

[34] W. Alabiso and S. Schlögl, "The impact of vitrimers on the industry of the future: Chemistry, properties and sustainable forward-looking applications," *Polymers (Basel).*, vol. 12, no. 8, 2020, doi: 10.3390/POLYM12081660.

[35] L. C. Zhang, L. Y. Chen, and L. Wang, "Surface Modification of Titanium and Titanium Alloys: Technologies, Developments, and Future Interests," *Adv. Eng. Mater.*, vol. 22, no. 5, 2020, doi: 10.1002/adem.201901258.

[36] V. Fiore and A. Valenza, "Epoxy resins as a matrix material in advanced fiber-reinforced polymer (FRP) composites," *Adv. Fibre-Reinforced Polym. Compos. Struct. Appl.*, pp. 88–121, 2013, doi: 10.1533/9780857098641.1.88.

[37] Y. Zhang *et al.*, "Flexible electronics based on micro/nanostructured paper," *Adv. Mater.*, vol. 30, no. 51, 2018, doi: 10.1002/adma.201801588.

[38] A. M. El-Shamy, "A review on: Biocidal activity of some chemical structures and their role in mitigation of microbial corrosion," *Egypt. J. Chem.*, vol. 63, no. 12,

pp. 5251–5267, 2020, doi: 10.21608/ejchem.2020.32160.2683.

[39] J. Liu, G. D. Howard, S. H. Lewis, M. D. Barros, and J. W. Stansbury, "A study of shrinkage stress reduction and mechanical properties of nanogel-modified resin systems," *Eur. Polym. J.*, vol. 48, no. 11, pp. 1819–1828, 2012, doi: 10.1016/j.eurpolymj.2012.08.009.

[40] L. G. Lovell, H. Lu, J. E. Elliott, J. W. Stansbury, and C. N. Bowman, "The effect of cure rate on the mechanical properties of dental resins," *Dent. Mater.*, vol. 17, no. 6, pp. 504–511, 2001, doi: 10.1016/S0109-5641(01)00010-0.

[41] Steelfab, "Uniform Attack Corrosion & Preventing Rust | Steel Fabrication Services," 2021. https://steelfabservices.com.au/uniform-attack-corrosion/ (accessed Dec. 02, 2023).

[42] Z. N. Azwa, B. F. Yousif, A. C. Manalo, and W. Karunasena, "A review on the degradability of polymeric composites based on natural fibres," *Mater. Des.*, vol. 47, pp. 424–442, 2013, doi: 10.1016/j.matdes.2012.11.025.

[43] G. Lazorenko, A. Kasprzhitskii, and T. Nazdracheva, "Anti-corrosion coatings for protection of steel railway structures exposed to atmospheric environments: A review," *Constr. Build. Mater.*, vol. 288, 2021, doi: 10.1016/j.conbuildmat.2021.123115.

[44] G. S. Frankel *et al.*, "A comparative review of the aqueous corrosion of glasses, crystalline ceramics, and metals," *npj Mater. Degrad.*, vol. 2, no. 1, p. 15, 2018, doi: 10.1038/s41529-018-0037-2.

[45] I. B. Beech and J. Sunner, "Biocorrosion: Towards understanding interactions between biofilms and metals," *Curr. Opin. Biotechnol.*, vol. 15, no. 3, pp. 181–186, 2004, doi: 10.1016/j.copbio.2004.05.001.

[46] S. M. Abd El Haleem, S. Abd El Wanees, E. E. Abd El Aal, and A. Diab, "Environmental factors affecting the corrosion behavior of reinforcing steel II. Role of some anions in the initiation and inhibition of pitting corrosion of steel in Ca(OH)2 solutions," *Corros. Sci.*, vol. 52, no. 2, pp. 292–302, 2010, doi: 10.1016/j.corsci.2009.09.004.

[47] A. Joshi and D. F. Stein, "Chemistry of Grain Boundaries and Its Relation To Intergranular Corrosion of Austenitic Stainless Steel.," *Corrosion*, vol. 28, no. 9, pp. 321–330, 1972, doi: 10.5006/0010-9312-28.9.321.

[48] F. Norouzi Afshar, J. H. W. de Wit, H. Terryn, and J. M. C. Mol, "The effect of brazing process on microstructure evolution and corrosion performance of a modified AA4XXX/AA3XXX brazing sheet," *Corros. Sci.*, vol. 58, pp. 242–250, 2012, doi: 10.1016/j.corsci.2012.01.030.

[49] N. Adya, M. Alam, T. Ravindranath, A. Mubeen, and B. Saluja, "Corrosion in titanium dental implants: Literature review," *J. Indian Prosthodont. Soc.*, vol. 5, no. 3, pp. 126–131, 2005, doi: 10.4103/0972-4052.17104.

[50] J. Bhandari, F. Khan, R. Abbassi, V. Garaniya, and R. Ojeda, "Modelling of

pitting corrosion in marine and offshore steel structures - A technical review," *J. Loss Prev. Process Ind.*, vol. 37, pp. 39–62, 2015, doi: 10.1016/j.jlp.2015.06.008.

[51] R. Singh and N. B. Dahotre, "Corrosion degradation and prevention by surface modification of biometallic materials," *J. Mater. Sci. Mater. Med.*, vol. 18, no. 5, pp. 725–751, 2007, doi: 10.1007/s10856-006-0016-y.

[52] R. Jia, T. Unsal, D. Xu, Y. Lekbach, and T. Gu, "Microbiologically influenced corrosion and current mitigation strategies: A state of the art review," *Int. Biodeterior. Biodegrad.*, vol. 137, pp. 42–58, 2019, doi: 10.1016/j.ibiod.2018.11.007.

[53] U. K. Chatterjee, S. K. Bose, and S. K. Roy, *Environmental Degradation of Metals*. CRC Press, 2001. doi: 10.1201/9781482292244.

[54] B. N. Popov, *Corrosion Engineering: Principles and Solved Problems*. Elsevier, 2015. doi: 10.1016/C2012-0-03070-0.

[55] R. Yee and L. Myers, "Enhanced tf40b gas turbine engine design changes to improve resistance to the Landing Craft Air Cushion (LCAC) operational environment," in *American Society of Mechanical Engineers, International Gas Turbine Institute, Turbo Expo (Publication) IGTI*, 2003, pp. 495–499. doi: 10.1115/GT2003-38714.

[56] D. A. Shifler, "Marine fasteners," *La Que's Handb. Mar. Corros.*, pp. 653–666, 2021, doi: 10.1002/9781119788867.ch23.

[57] S. S. Prabha *et al.*, "Corrosion Problems in Petroleum Industry and their solution," *Eur. Chem. Bull.*, vol. 3, no. 3, pp. 300–307, 2014, [Online]. Available: http://www.eurchembull.com/index.php/ECB/article/view/1334

[58] K. A. Chandler, *Marine and Offshore Corrosion: Marine Engineering Series*. Elsevier, 2014. [Online]. Available: https://books.google.com/books?id=QiKjBQAAQBAJ&pgis=1

[59] P. Kumar and B. Imam, "Footprints of air pollution and changing environment on the sustainability of built infrastructure," *Sci. Total Environ.*, vol. 444, pp. 85–101, 2013, doi: 10.1016/j.scitotenv.2012.11.056.

[60] "Salt spray: how to protect marine electronics from salt, salt fog,…." https://www.dolphin-charger.com/news/salt-spray-protect-marine-electronics (accessed Dec. 02, 2023).

[61] I. L. ROSENFELD and I. K. MARSHAKOV, "Mechanism of Crevice Corrosion," *Corrosion*, vol. 20, no. 4, pp. 115t-125t, 1964, doi: 10.5006/0010-9312-20.4.115t.

[62] S. Natarajan, V. Sivan, P. G. Tennyson, and V. R. Kiran, "Protective coatings on magnesium and its alloys: A critical review," *Corros. Prev. Control*, vol. 51, no. 4, pp. 142–163, 2004.

[63] N. K. Akafuah, S. Poozesh, A. Salaimeh, G. Patrick, K. Lawler, and K. Saito, "Evolution of the automotive body coating process-A review," *Coatings*, vol. 6,

no. 2, p. 24, 2016, doi: 10.3390/coatings6020024.

[64] S. S. Pathak, S. K. Mendon, M. D. Blanton, and J. W. Rawlins, “Magnesium-Based sacrificial anode cathodic protection coatings (Mg-Rich primers) for aluminum alloys,” *Metals (Basel).*, vol. 2, no. 3, pp. 353–376, 2012, doi: 10.3390/met2030353.

[65] R. B. Polder, G. Leegwater, D. Worm, and W. Courage, “Service life and life cycle cost modelling of cathodic protection systems for concrete structures,” *Cem. Concr. Compos.*, vol. 47, pp. 69–74, 2014, doi: 10.1016/j.cemconcomp.2013.05.004.

[66] J. Zhang, C. Deng, J. Song, C. Deng, M. Liu, and K. Zhou, “MoB-CoCr as alternatives to WC-12Co for stainless steel protective coating and its corrosion behavior in molten zinc,” *Surf. Coatings Technol.*, vol. 235, pp. 811–818, 2013, doi: 10.1016/j.surfcoat.2013.08.052.

[67] J. Sun *et al.*, “Direct low-temperature synthesis of graphene on various glasses by plasma-enhanced chemical vapor deposition for versatile, cost-effective electrodes,” *Nano Res.*, vol. 8, no. 11, pp. 3496–3504, 2015, doi: 10.1007/s12274-015-0849-0.

[68] S. Buapool, N. Thavarungkul, N. Srisukhumbowornchai, and P. Termsuksawad, “Modeling and Analysis of the Effect of Dip-Spin Coating Process Parameters on Coating Thickness Using Factorial Design Method,” *Adv. Mater. Sci. Eng.*, vol. 2017, 2017, doi: 10.1155/2017/9639306.

[69] H. Sojoudi, M. Wang, N. D. Boscher, G. H. McKinley, and K. K. Gleason, “Durable and scalable icephobic surfaces: Similarities and distinctions from superhydrophobic surfaces,” *Soft Matter*, vol. 12, no. 7, pp. 1938–1963, 2016, doi: 10.1039/c5sm02295a.

[70] “Precision dip coating for the fabrication of thin films | Engineer Live.” http://www.engineerlive.com/content/21225 (accessed Dec. 02, 2023).

[71] L. C. de F. Gomes, H. C. Gomes, and E. D. Reis, “Surface Waterproofing Techniques: A Case Study in Nova Lima, Brazil,” *Eng*, vol. 4, no. 3, pp. 1871–1890, 2023.

[72] D. W. Lee *et al.*, “A solution-derived bismuth aluminum gallium tin oxide film constructed by a brush coating method for spontaneous liquid crystal alignment,” *Mater. Adv.*, vol. 3, no. 14, pp. 6019–6027, 2022, doi: 10.1039/d2ma00421f.

[73] P. Khullar, *Development and implementation of novel bristle tool for surface treatment of metallic components*. Marquette University, 2009.

[74] R. Leach, *The Printing Ink Manual*. Springer Science & Business Media, 1988. doi: 10.1007/978-94-011-7097-0.

[75] E. Shim, “Coating and laminating processes and techniques for textiles,” *Smart Text. Coatings Laminates*, pp. 11–45, Jan. 2018, doi: 10.1016/B978-0-08-102428-7.00002-X.

[76] J. Li, J. Fleetwood, W. B. Hawley, and W. Kays, "From Materials to Cell: State-of-the-Art and Prospective Technologies for Lithium-Ion Battery Electrode Processing," *Chem. Rev.*, vol. 122, no. 1, pp. 903–956, 2022, doi: 10.1021/acs.chemrev.1c00565.

[77] F. Burbulla *et al.*, "Modelling of Adhesively Bonded Joints in CAE-Models at Porsche–Look behind the Scenes," in *11th EUROPEAN LS-DYNA CONFERENCE*, 2017, p. 37.

[78] "Coatings 101: Everything You Need to Know About Plasma Spray Coating." https://www.industrialcoat.com/coatings-101-everything-you-need-to-know-about-plasma-spray-coating/ (accessed Dec. 02, 2023).

[79] N. Dey, S. Majumdar, and M. Rao, "Multiparticulate Drug Delivery Systems for Controlled Release," *Trop. J. Pharm. Res.*, vol. 7, no. 3, pp. 1067–1075, 2008, doi: 10.4314/tjpr.v7i3.14692.

[80] D. Mao, G. Lv, G. Gao, and B. Fan, "Fabrication of polyimide films with imaging quality using a spin-coating method for potential optical applications," *J. Polym. Eng.*, vol. 39, no. 10, pp. 917–925, 2019, doi: 10.1515/polyeng-2019-0177.

[81] G. George, Sivasankara Rao Ede, and Zhiping Luo, "Spin Coating - Fundamentals of Perovskite Oxides: Synthesis, Structure, Properties and Applications," *CRC Press*, 2020. https://ebrary.net/191967/engineering/spin_coating (accessed Dec. 02, 2023).

[82] O. and C. C. Association and O. and C. C. Association, "Industrial Coatings: Application and Curing Methods," *Surf. Coatings Vol 2-Paints their Appl.*, pp. 718–747, 1984.

[83] M. Joshi and B. S. Butola, "Application technologies for coating, lamination and finishing of technical textiles," in *Advances in the Dyeing and Finishing of Technical Textiles*, Elsevier, 2013, pp. 355–411. doi: 10.1533/9780857097613.2.355.

[84] "Schematic-representation-of-flow-coating-process-used-to-prepare-MSPs-and-MSBCPs-The."

[85] A. A. Nazeer and M. Madkour, "Potential use of smart coatings for corrosion protection of metals and alloys: A review," *J. Mol. Liq.*, vol. 253, pp. 11–22, 2018, doi: 10.1016/j.molliq.2018.01.027.

[86] A. Wang, K. De Silva, M. Jones, P. Robinson, G. Larribe, and W. Gao, "Anticorrosive coating systems for marine propellers," *Prog. Org. Coatings*, vol. 183, p. 107768, 2023, doi: 10.1016/j.porgcoat.2023.107768.

[87] S. G. Croll, "Stress and embrittlement in organic coatings during general weathering exposure: A review," *Prog. Org. Coatings*, vol. 172, p. 107085, 2022, doi: 10.1016/j.porgcoat.2022.107085.

[88] Wei B M, "Metal Corrosion Theory and Application," *Press Chem. Ind. Peking*, 1984.

[89] R. E. Melchers, “Microbiological and abiotic processes in modelling longer-term marine corrosion of steel,” *Bioelectrochemistry*, vol. 97, pp. 89–96, 2014, doi: 10.1016/j.bioelechem.2013.07.002.

[90] M. Zhang, L. Ma, L. Wang, Y. Sun, and Y. Liu, “Insights into the Use of Metal-Organic Framework As High-Performance Anticorrosion Coatings,” *ACS Appl. Mater. Interfaces*, vol. 10, no. 3, pp. 2259–2263, 2018, doi: 10.1021/acsami.7b18713.

[91] “Blue SandBlasting Stainless Steel Sheet - BMJ Metal CO., LTD.” https://www.bmjmetal.com/product/blue-sand-blasting-stainless-steel-sheet/ (accessed Dec. 02, 2023).

[92] H. Park *et al.*, “Zeolitic imidazolate framework-67 (ZIF-67) rhombic dodecahedrons as full-spectrum light harvesting photocatalyst for environmental remediation,” *Solid State Sci.*, vol. 62, pp. 82–89, 2016, doi: 10.1016/j.solidstatesciences.2016.10.018.

[93] A. M. Mohamed, W. A. Abbas, G. E. Khedr, W. Abass, and N. K. Allam, “Computational and experimental elucidation of the boosted stability and antibacterial activity of ZIF-67 upon optimized encapsulation with polyoxometalates,” *Sci. Rep.*, vol. 12, no. 1, p. 15989, 2022, doi: 10.1038/s41598-022-20392-4.

[94] Y. Lei *et al.*, “Preparation of ZIF-67@DTMS NPs/Epoxy composite coating and its anti-corrosion performance for Q235 carbon steel in 3.5 wt% NaCl solution,” *Colloids Surfaces A Physicochem. Eng. Asp.*, vol. 656, p. 130370, 2023, doi: 10.1016/j.colsurfa.2022.130370.

[95] L. Larby and A. Lundberg, “Primary Study of the Phase Relationship in the MgO-" V2O3" System at 1873 K and pO2= 10-11 atm.” 2018.

[96] MD. ABDULLAH AL MASUD et al, “ANALYZING THE EFFECT OF ANNEALING TEMPERATURE ON THE CRYSTALLINE PARAMETERS OF ZnO NANOPARTICLES,” no. November 2019, p. 89, 2019.

[97] C. Maria, “Application of FTIR Spectroscopy in Environmental Studies,” *Adv. Asp. Spectrosc.*, vol. 29, no. 1, pp. 77–86, 2012, doi: 10.5772/48331.

[98] A. A. Ismail, F. R. van de Voort, and J. Sedman, “Chapter 4 Fourier transform infrared spectroscopy: Principles and applications,” in *Techniques and Instrumentation in Analytical Chemistry*, Elsevier, 1997, pp. 93–139. doi: 10.1016/S0167-9244(97)80013-3.

[99] X. Hou, S. Lv, Z. Chen, and F. Xiao, “Applications of Fourier transform infrared spectroscopy technologies on asphalt materials,” *Meas. J. Int. Meas. Confed.*, vol. 121, pp. 304–316, 2018, doi: 10.1016/j.measurement.2018.03.001.

[100] R. R. Mather, “Surface modification of textiles by plasma treatments,” *Surf. Modif. Text.*, pp. 296–317, 2009, doi: 10.1533/9781845696689.296.

[101] O. J. Guy and K. A. D. Walker, “Graphene Functionalization for Biosensor

Applications," *Silicon Carbide Biotechnol. A Biocompatible Semicond. Adv. Biomed. Devices Appl. Second Ed.*, pp. 85–141, 2016, doi: 10.1016/B978-0-12-802993-0.00004-6.

[102] H. Bluhm, "X-ray photoelectron spectroscopy (XPS) for in situ characterization of thin film growth," *Situ Charact. Thin Film Growth*, pp. 75–98, 2011, doi: 10.1533/9780857094957.2.75.

[103] H. Konno, "X-ray Photoelectron Spectroscopy," *Mater. Sci. Eng. Carbon Charact.*, pp. 153–171, 2016, doi: 10.1016/B978-0-12-805256-3.00008-8.

[104] E. B. Bahadir and M. K. Sezgintürk, "A review on impedimetric biosensors," *Artif. Cells, Nanomedicine Biotechnol.*, vol. 44, no. 1, pp. 248–262, 2016, doi: 10.3109/21691401.2014.942456.

[105] L. D. Ha, K. Park, B. Y. Chang, and S. Hwang, "Implementation of Second-Generation Fourier Transform Electrochemical Impedance Spectroscopy with Commercial Potentiostat and Application to Time-Resolved Electrochemical Impedance Spectroscopy," *Anal. Chem.*, 2019, doi: 10.1021/acs.analchem.9b03226.

[106] E. Katz and I. Willner, "Probing biomolecular interactions at conductive and semiconductive surfaces by impedance spectroscopy: Routes to impedimetric immunosensors, DNA-sensors, and enzyme biosensors," *Electroanalysis*, vol. 15, no. 11, pp. 913–947, 2003, doi: 10.1002/elan.200390114.

[107] F. Fasmin and R. Srinivasan, "Review—Nonlinear Electrochemical Impedance Spectroscopy," *J. Electrochem. Soc.*, vol. 164, no. 7, pp. H443–H455, 2017, doi: 10.1149/2.0391707jes.

[108] M. I. Prodromidis, "Impedimetric immunosensors-A review," *Electrochim. Acta*, vol. 55, no. 14, pp. 4227–4233, 2010, doi: 10.1016/j.electacta.2009.01.081.

[109] A. Lasia, "Impedance of the Faradaic Reactions in the Presence of Adsorption," *Electrochem. Impedance Spectrosc. its Appl.*, pp. 127–145, 2014, doi: 10.1007/978-1-4614-8933-7_5.

[110] A. Lasia, "Definition of Impedance and Impedance of Electrical Circuits," *Electrochem. Impedance Spectrosc. its Appl.*, pp. 7–66, 2014, doi: 10.1007/978-1-4614-8933-7_2.

[111] S. Wang, J. Zhang, O. Gharbi, V. Vivier, M. Gao, and M. E. Orazem, "Electrochemical impedance spectroscopy," *Nat. Rev. Methods Prim.*, vol. 1, no. 1, 2021, doi: 10.1038/s43586-021-00039-w.

[112] N. Anita *et al.*, "Linear polarization resistance (LPR) technique for corrosion measurements," in *Electrochemical and Analytical Techniques for Sustainable Corrosion Monitoring: Advances, Challenges and Opportunities*, Elsevier, 2023, pp. 59–80. doi: 10.1016/B978-0-443-15783-7.00005-0.

[113] J. Qian, F. Sun, and L. Qin, "Hydrothermal synthesis of zeolitic imidazolate framework-67 (ZIF-67) nanocrystals," *Mater. Lett.*, vol. 82, pp. 220–223, 2012,

doi: 10.1016/j.matlet.2012.05.077.

[114] R. M. Abdelhameed and M. El-Shahat, “Fabrication of ZIF-67@MIL-125-NH2 nanocomposite with enhanced visible light photoreduction activity,” *J. Environ. Chem. Eng.*, vol. 7, no. 3, 2019, doi: 10.1016/j.jece.2019.103194.

[115] S. Afzal, S. Tehreem, T. Munir, S. G. Sarwar, and I. L. Ikhioya, “Impact of Transition Metal Doped Bismuth Oxide Nanocomposites on the Bandgap Energy for Photoanode Application,” vol. 2, no. 1, pp. 104–109, 2023.

[116] K. Sethuraman and M. Alagar, “Thermo-mechanical and dielectric properties of graphene reinforced caprolactam cardanol based benzoxazine-epoxy nanocomposites,” *RSC Adv.*, vol. 5, no. 13, pp. 9607–9617, 2015, doi: 10.1039/c4ra14383c.

[117] N. Boumedienne and A. Maaroufi, “Structural and opto-electronic properties of epoxy/silver nanocomposite films,” *Phys. B Condens. Matter*, vol. 578, no. November 2019, 2020, doi: 10.1016/j.physb.2019.411853.

[118] S. Thomas, R. Keshavamurthy, P. G. S. Kumar, V. Tambrallimath, and G. D. Prasanna, “An improved compocasting technique for uniformly dispersed multi-walled carbon nanotube in AA2219 Alloy Melt,” *FME Trans.*, vol. 48, no. 3, pp. 581–587, 2020, doi: 10.5937/fme2003581T.

[119] X. Xu *et al.*, “Effect of Mn content on microstructure and properties of 6000 series aluminum alloy,” *Appl. Phys. A Mater. Sci. Process.*, vol. 125, no. 8, pp. 1–9, 2019, doi: 10.1007/s00339-019-2780-9.

[120] R. Ediati, P. Elfianuar, E. Santoso, D. Oktavia Sulistiono, and M. Nadjib, “Synthesis of MCM-41/ZIF-67 Composite for Enhanced Adsorptive Removal of Methyl Orange in Aqueous Solution,” *Mesoporous Mater. - Prop. Appl.*, 2019, doi: 10.5772/intechopen.84691.

[121] S. Sundriyal, V. Shrivastav, H. Kaur, S. Mishra, and A. Deep, “High-Performance Symmetrical Supercapacitor with a Combination of a ZIF-67/rGO Composite Electrode and a Redox Additive Electrolyte,” *ACS Omega*, vol. 3, no. 12, pp. 17348–17358, 2018, doi: 10.1021/acsomega.8b02065.

[122] K. Saravanakumar, V. Arumugam, R. Souhith, and C. Santulli, “Influence of milled glass fiber fillers on mode I & mode II interlaminar fracture toughness of epoxy resin for fabrication of glass/epoxy composites,” *Fibers*, vol. 8, no. 6, 2020, doi: 10.3390/FIB8060036.

[123] X. Song *et al.*, “Ionic liquids-functionalized zeolitic imidazolate framework for carbon dioxide adsorption,” *Materials (Basel).*, vol. 12, no. 15, 2019, doi: 10.3390/ma12152361.

[124] S. Zhou *et al.*, “ZIF-67 MOF-derived Co nanoparticles supported on N-doped carbon skeletons for the amperometric determination of hydrogen peroxide,” *Microchim. Acta*, vol. 188, no. 11, 2021, doi: 10.1007/s00604-021-05020-8.